

Supporting Information: Nudged elastic band method for molecular reactions using energy-weighted springs combined with eigenvector following

Vilhjálmur Ásgeirsson,[†] Benedikt Orri Birgisson,[†] Ragnar Bjornsson,[‡] Ute Becker,[¶]
Frank Neese,[¶] Christoph Riplinger,[§] and Hannes Jónsson^{*,†}

[†]*Science Institute and Faculty of Physical Sciences, University of Iceland VR-III, 107
Reykjavík, Iceland*

[‡]*Max-Planck-Institute for Chemical Energy Conversion, Mülheim an der Ruhr 45470,
Germany.*

[¶]*Max-Planck-Institute for Kohlenforschung, Mülheim an der Ruhr 45470, Germany*

[§]*FaccTs GmbH, Rolandstrasse 67, 50677 Cologne, Germany*

E-mail: hj@hi.is

SI-1 A large and diverse benchmark set of molecular reactions

In this section, the benchmark set of 121 main-group molecular reactions used to evaluate the (EW-)CI-NEB and NEB-TS methods is introduced.^{1,2} The reactant, product and saddle point configurations are visualized. Modifications made to the reactant and product configurations are addressed. The potential energy barrier height, absolute imaginary frequency at the first order saddle points and reaction energy are given. As discussed in the Article, all calculations use B3LYP+D3(BJ)/def2-SVP level of theory.

SI-1.1 Visualization of reactant and product configurations

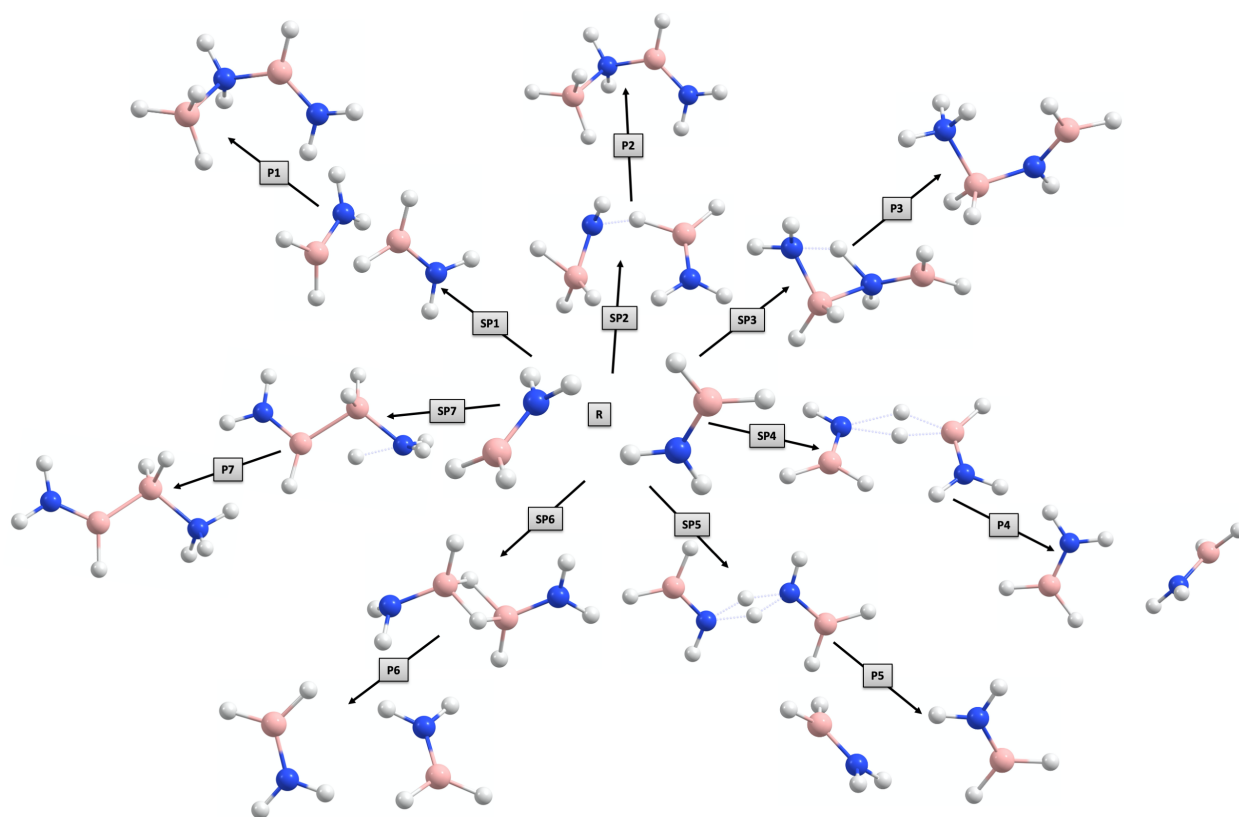


Figure 1: Reactant, saddle point and product configurations for reactions 1–7.

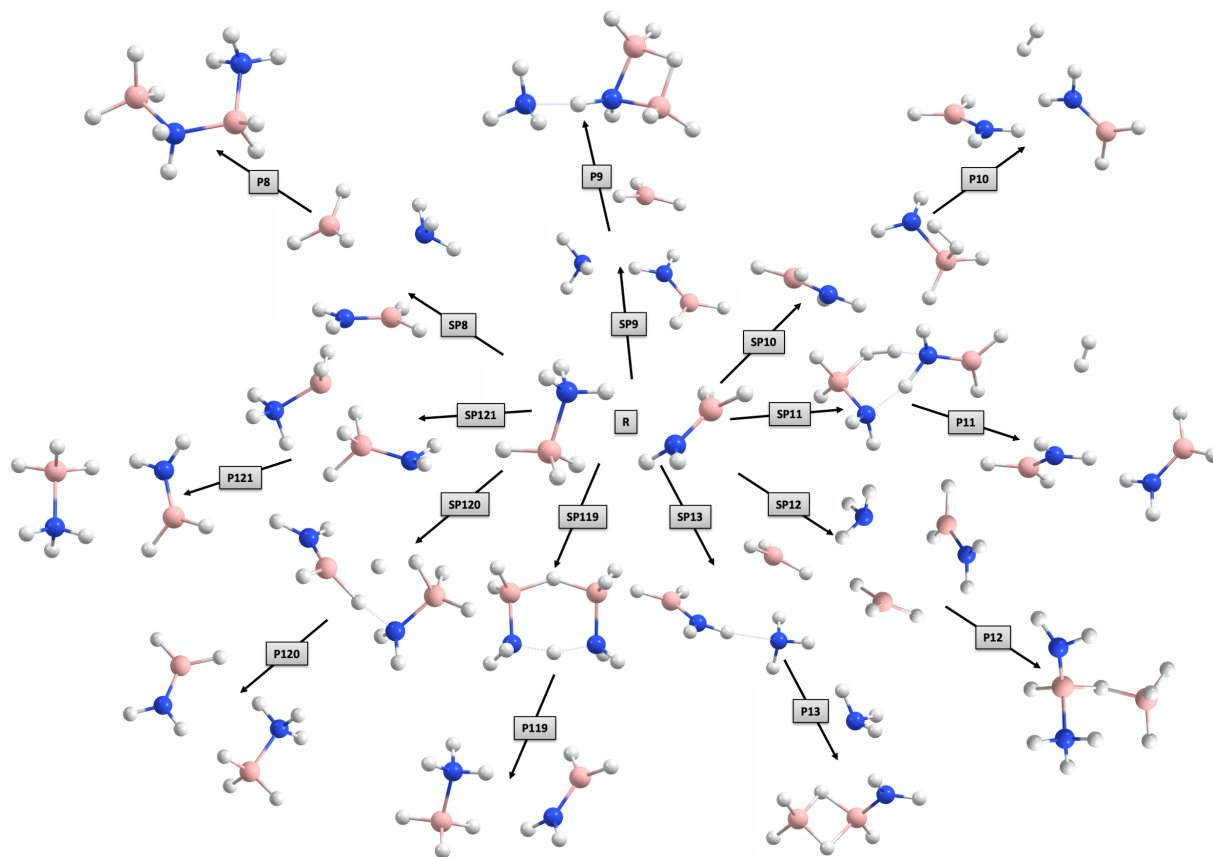


Figure 2: Reactant, saddle point and product configurations for reactions 8–13 and 119–121.

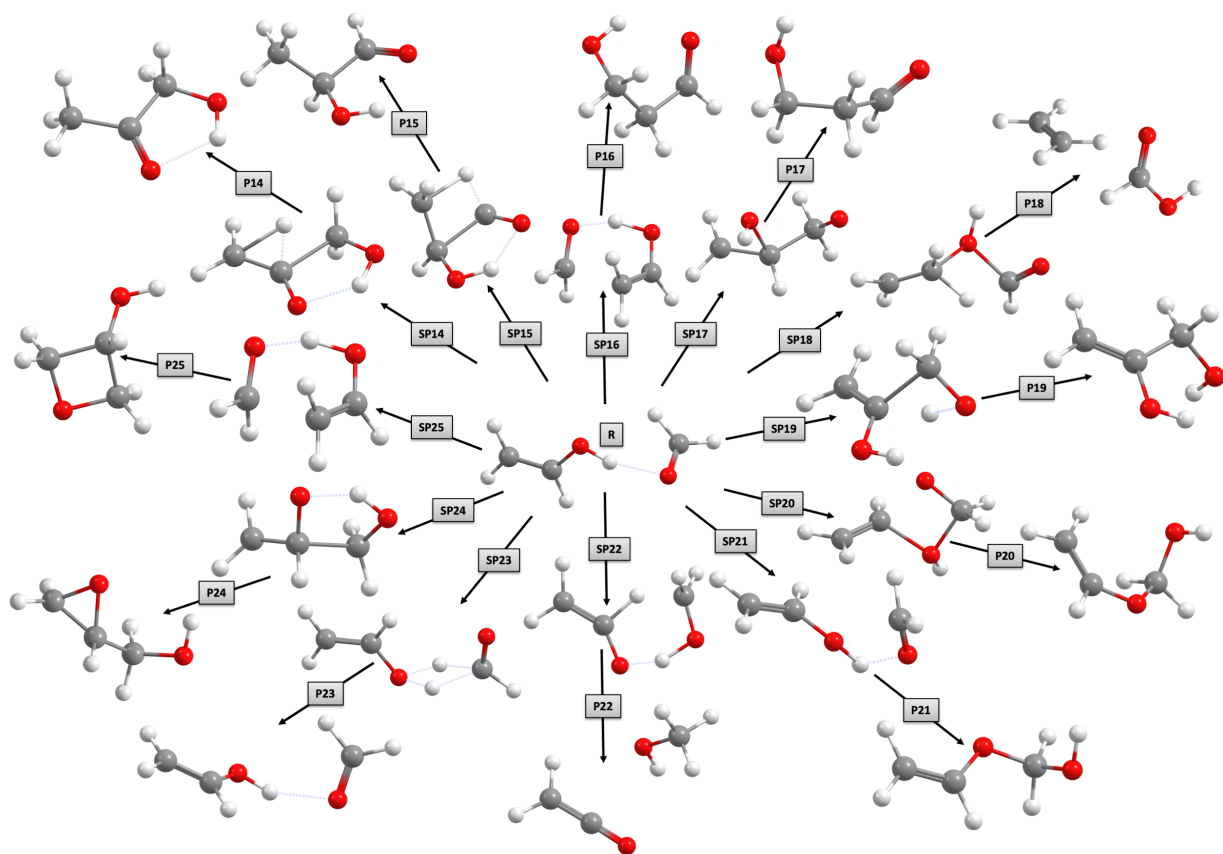


Figure 3: Reactant, saddle point and product configurations for reactions 14–25.

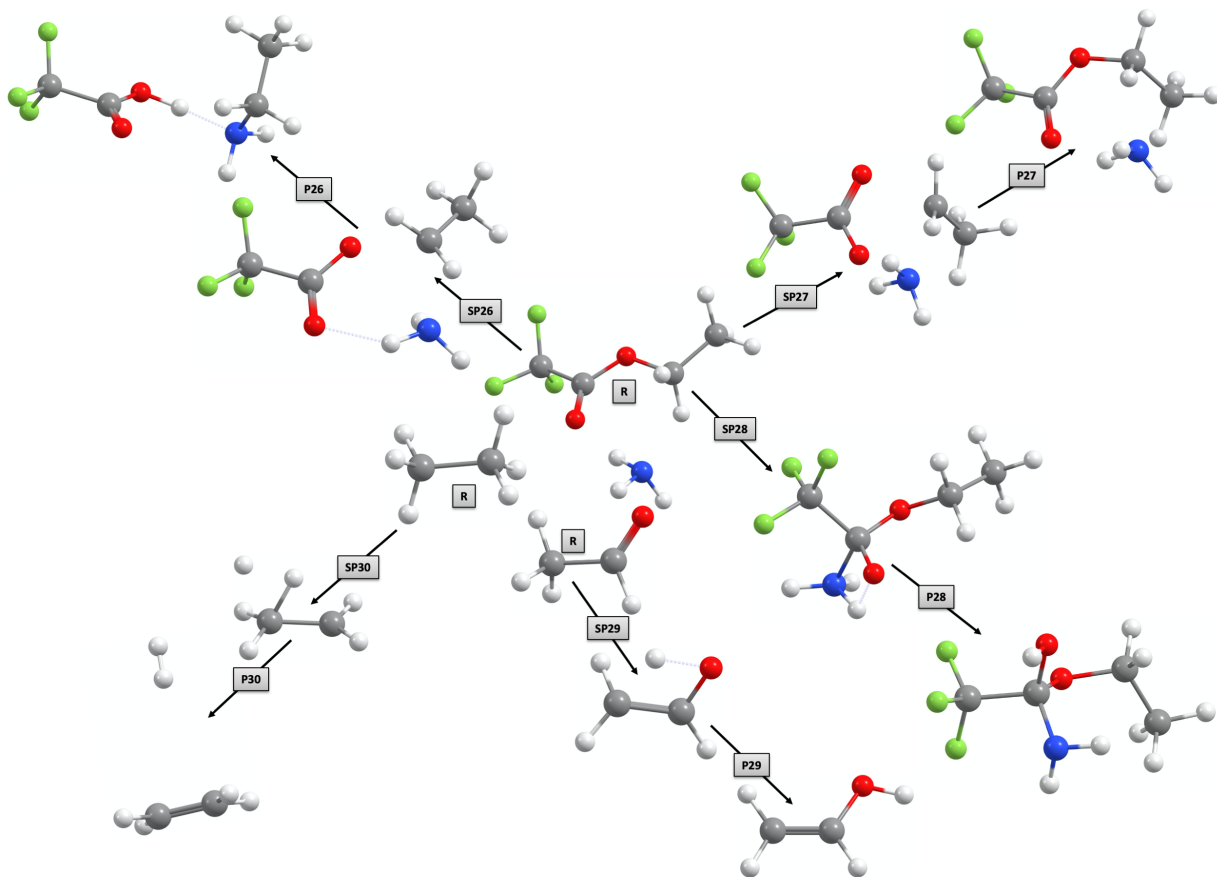


Figure 4: Reactant, saddle point and product configurations for reactions 26–30.

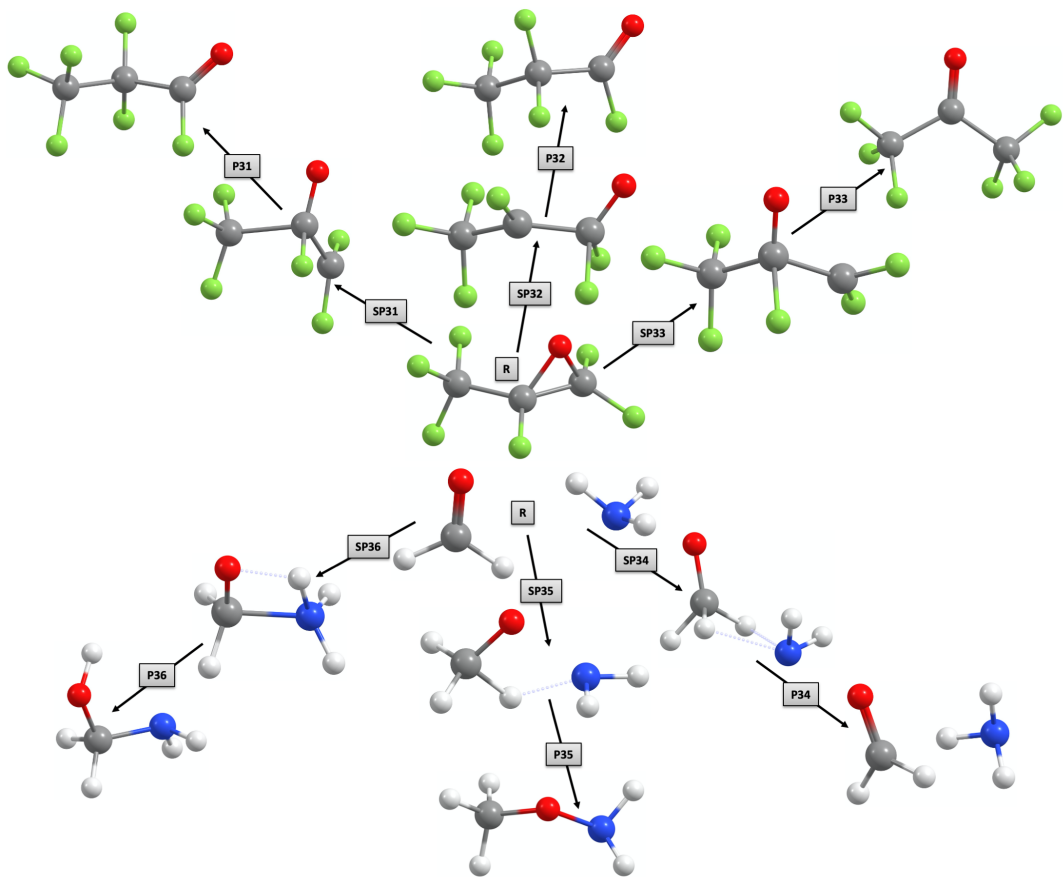


Figure 5: Reactant, saddle point and product configurations for reactions 31–36.

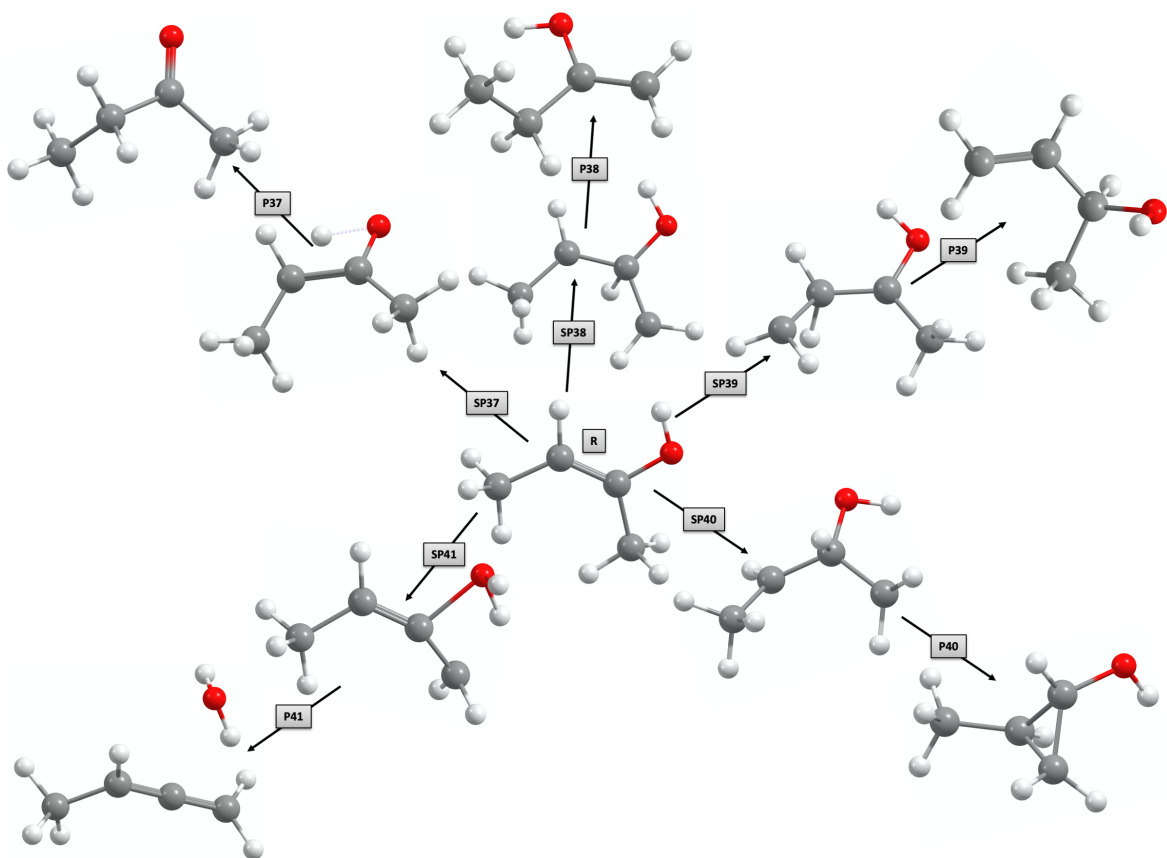


Figure 6: Reactant, saddle point and product configurations for reactions 37–41.

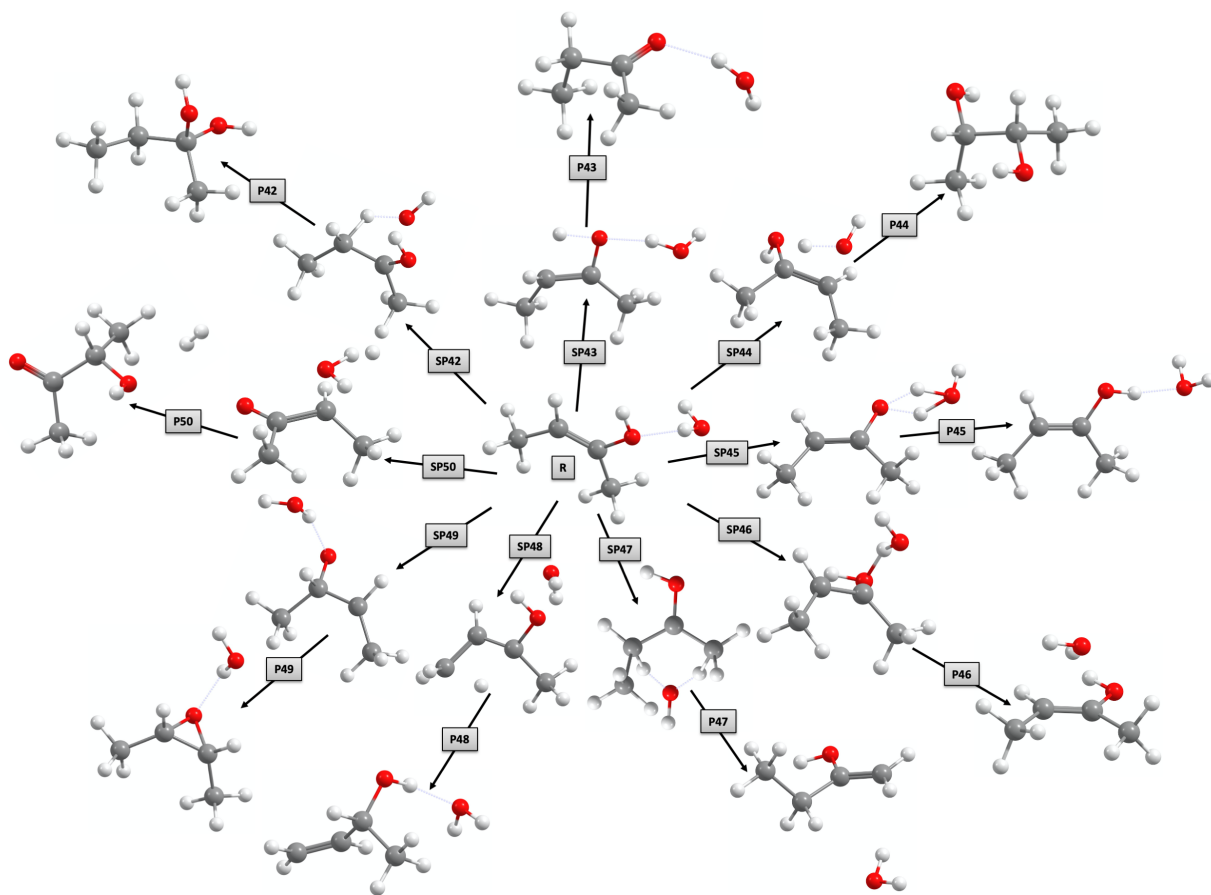


Figure 7: Reactant, saddle point and product configurations for reactions 42–50.

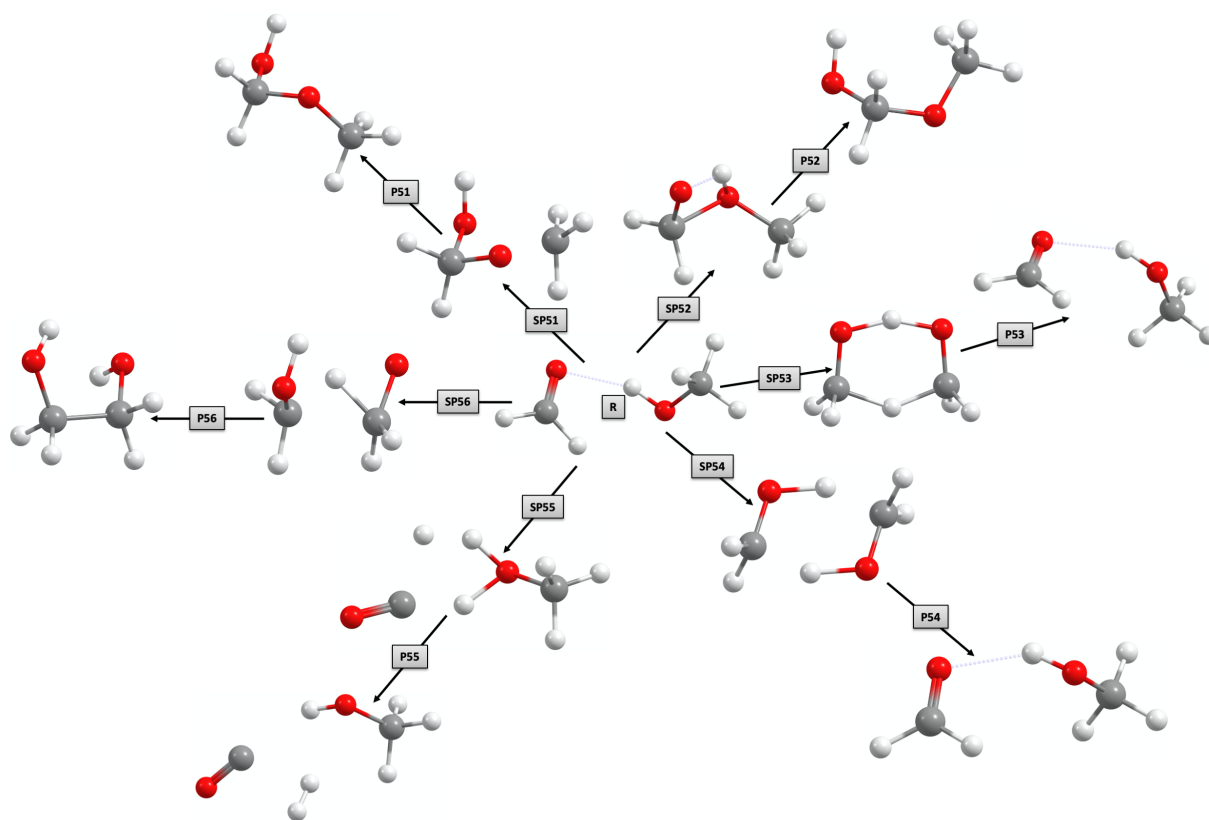


Figure 8: Reactant, saddle point and product configurations for reactions 51–56.

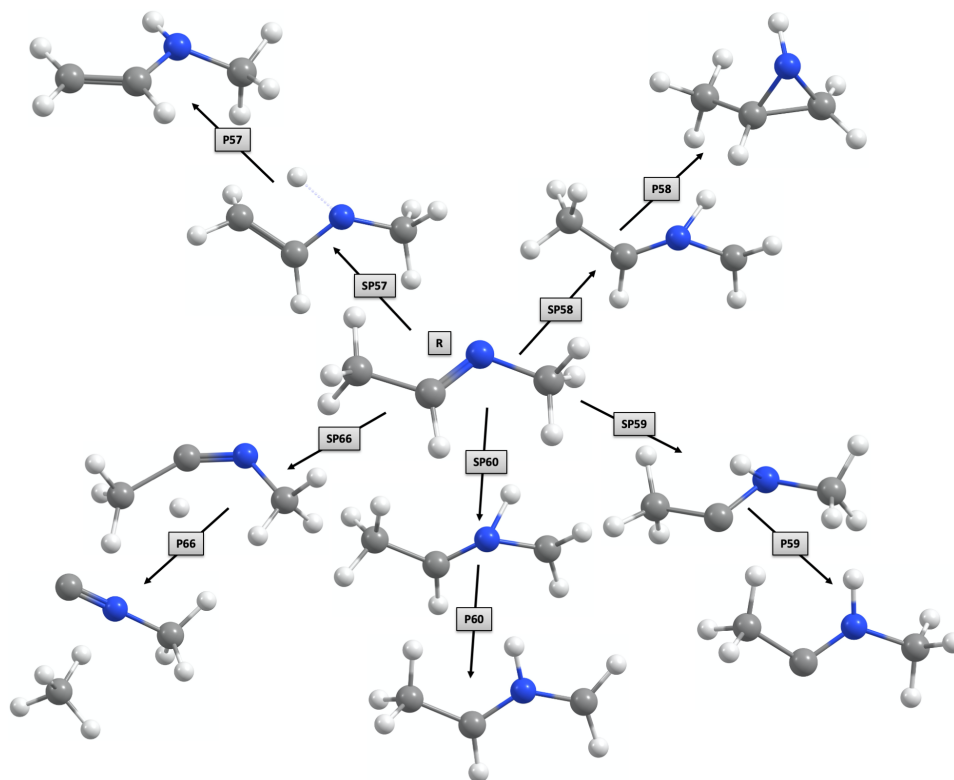


Figure 9: Reactant, saddle point and product configurations for reactions 57–59, 60 and 66.

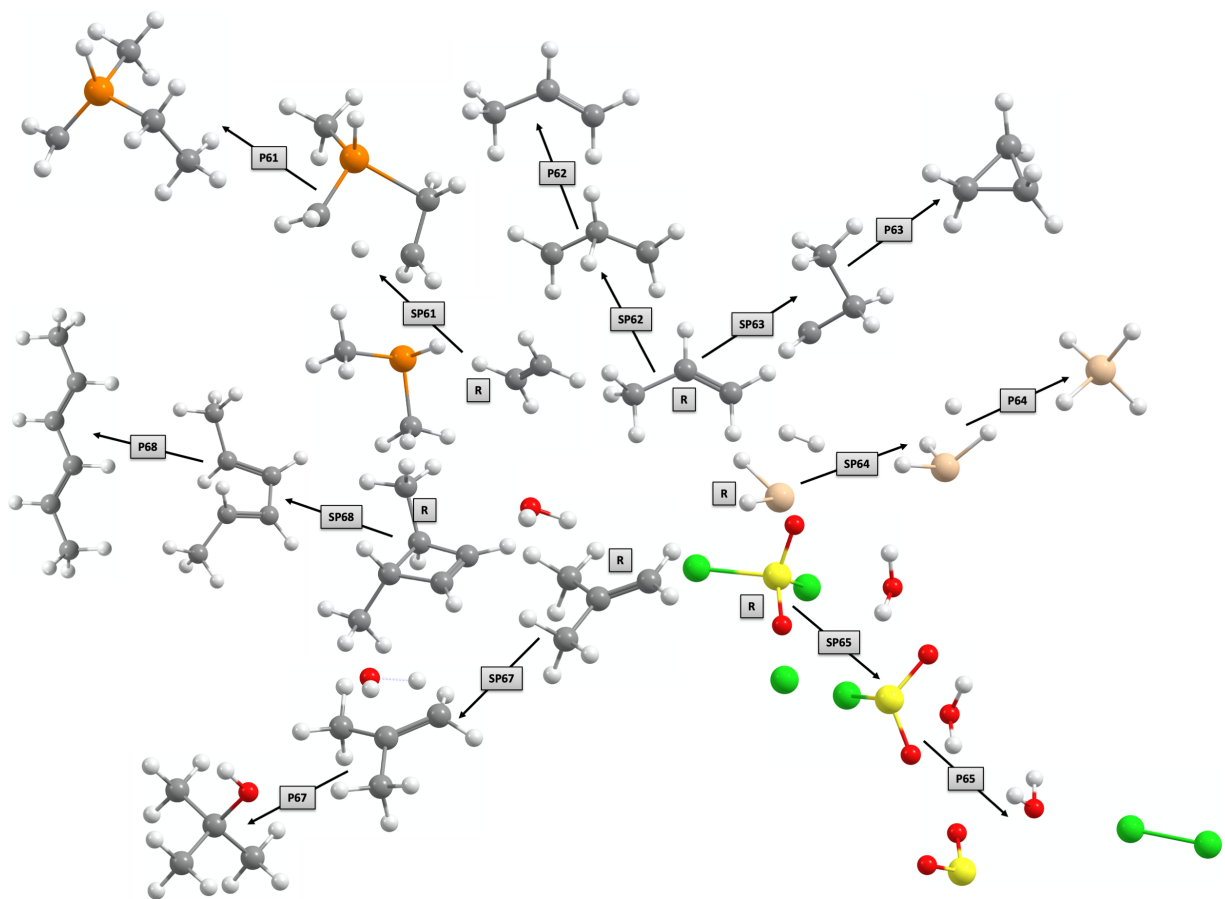


Figure 10: Reactant, saddle point and product configurations for reactions 61–65, 67 and 68.

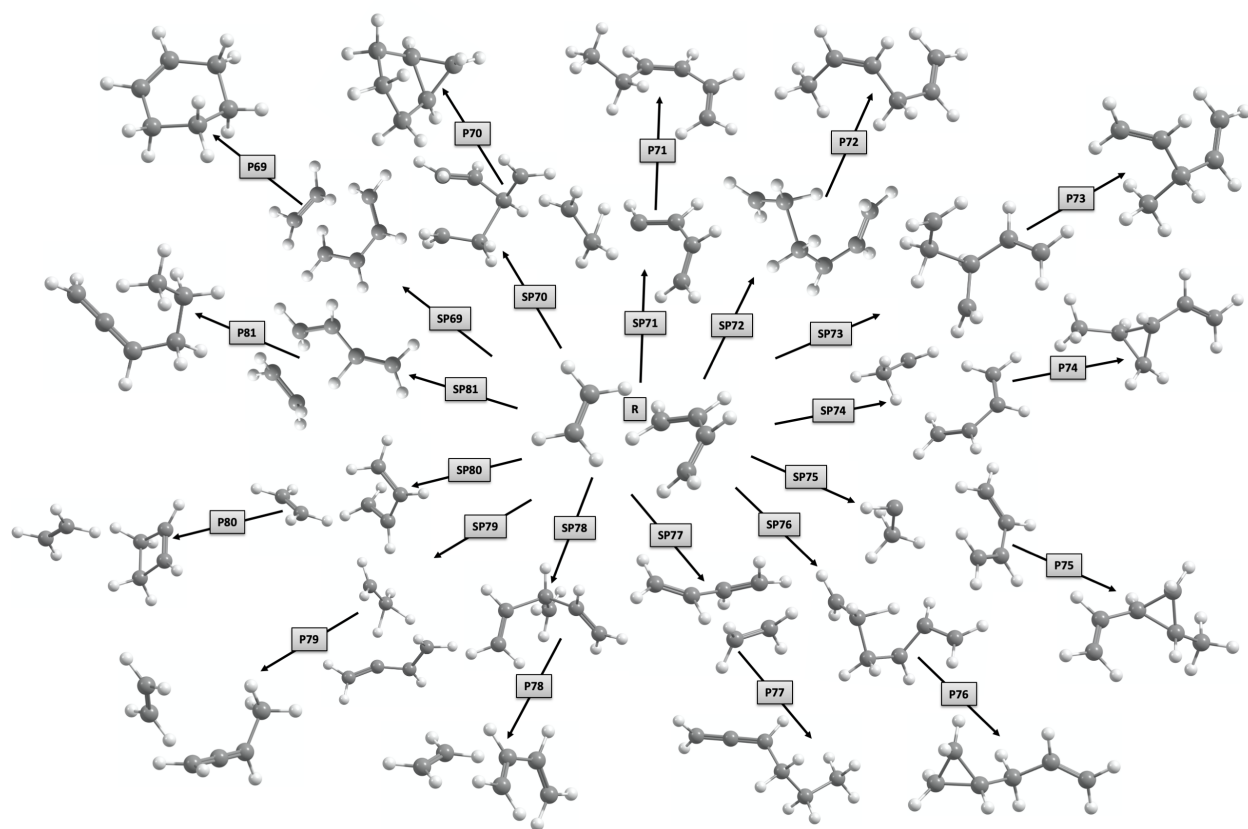


Figure 11: Reactant, saddle point and product configurations for reactions 69–81.

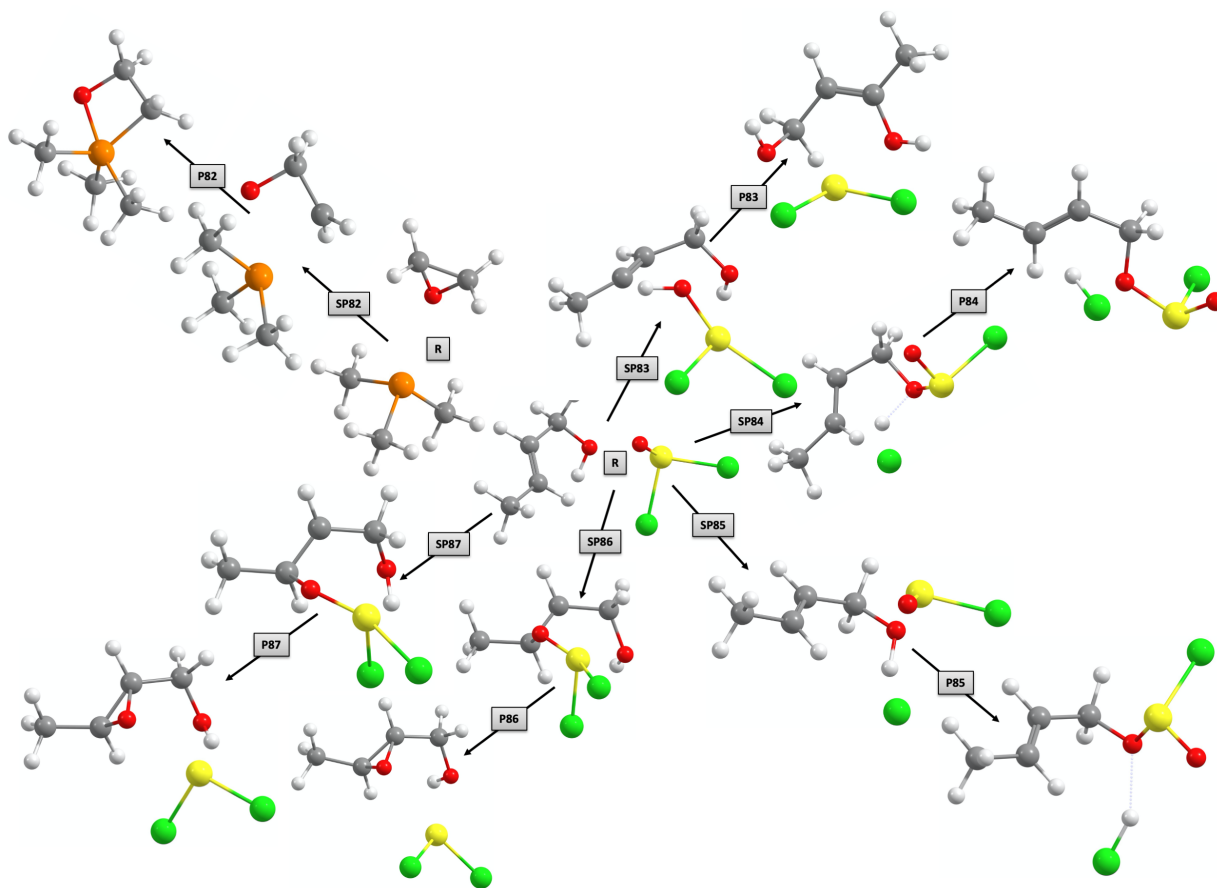


Figure 12: Reactant, saddle point and product configurations for reactions 82–87.

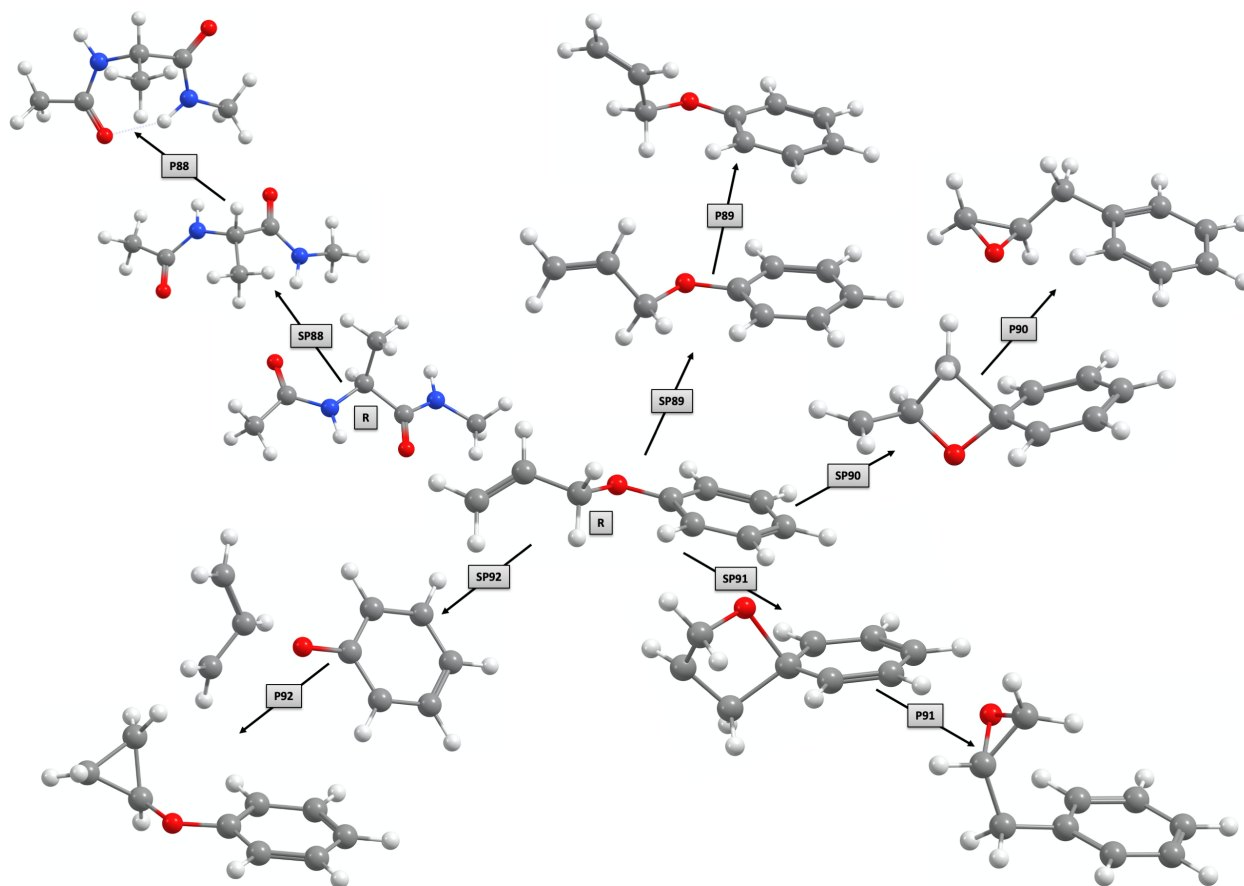


Figure 13: Reactant, saddle point and product configurations for reactions 88–92.

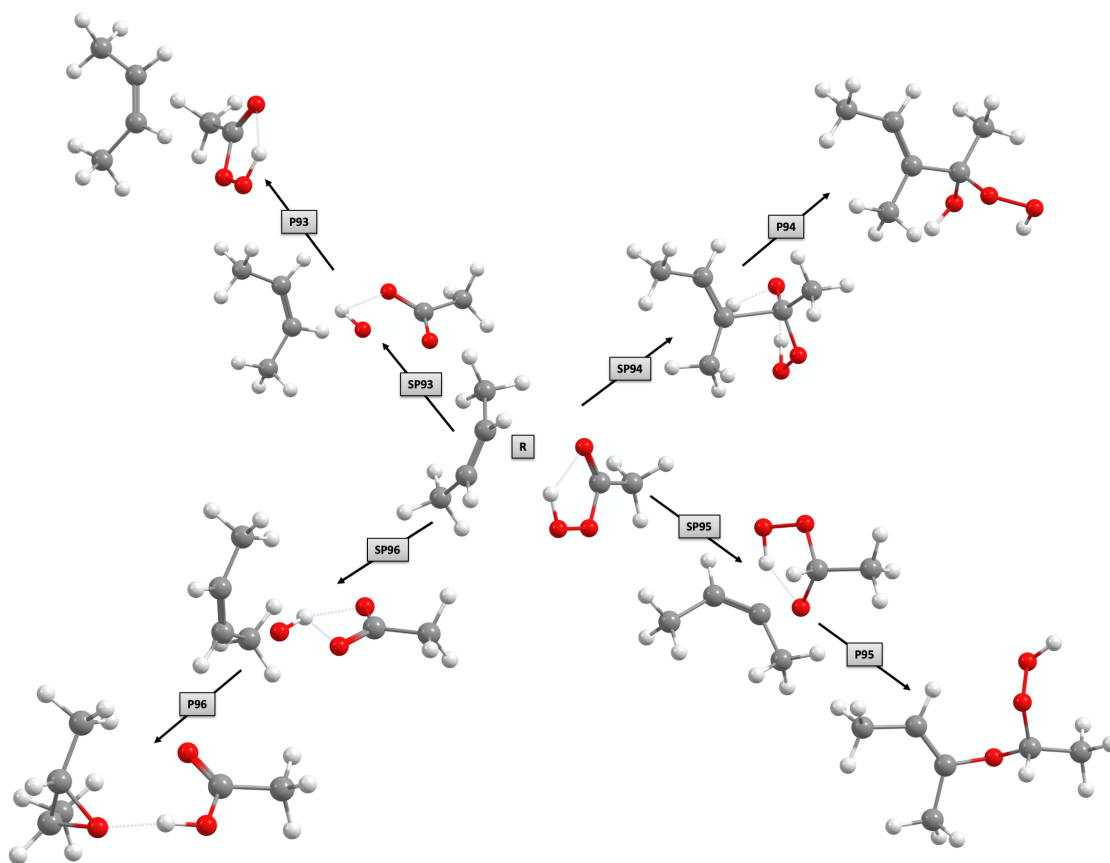


Figure 14: Reactant, saddle point and product configurations for reactions 93–96.

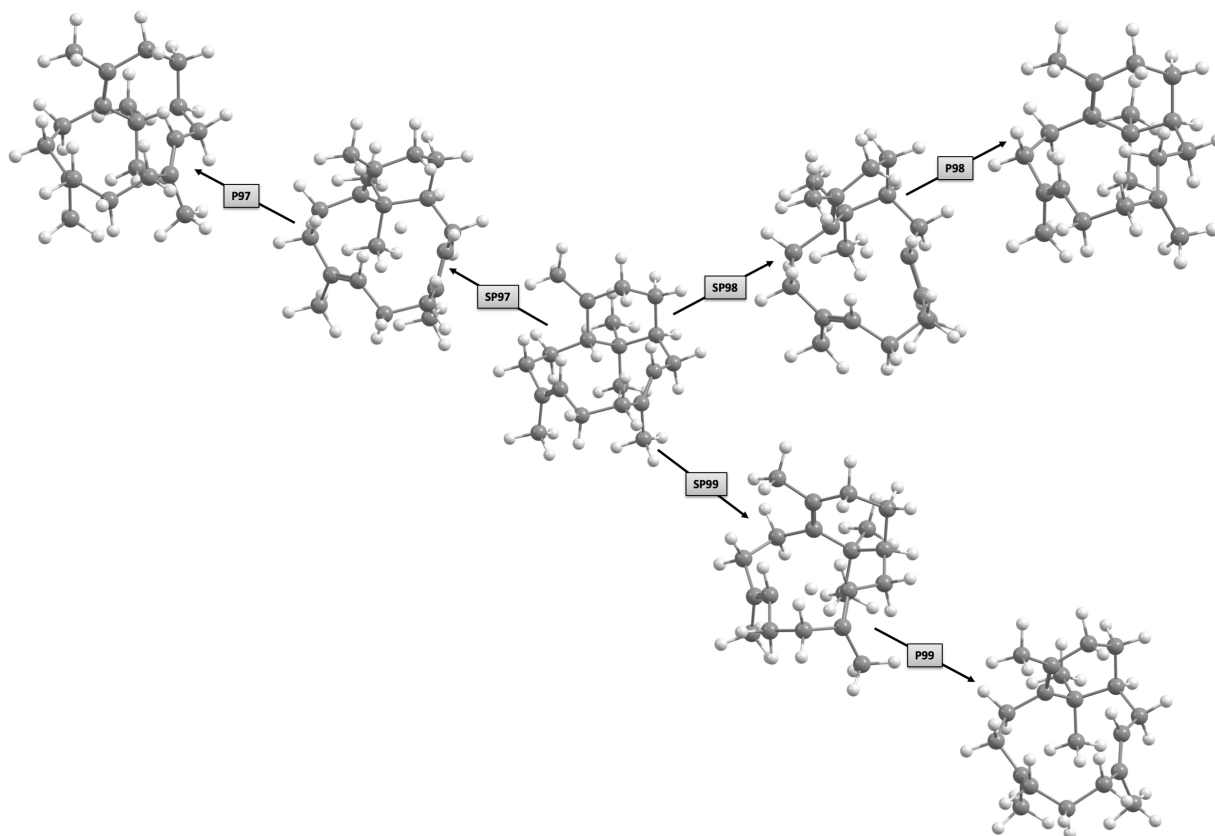


Figure 15: Reactant, saddle point and product configurations for reactions 97–99.

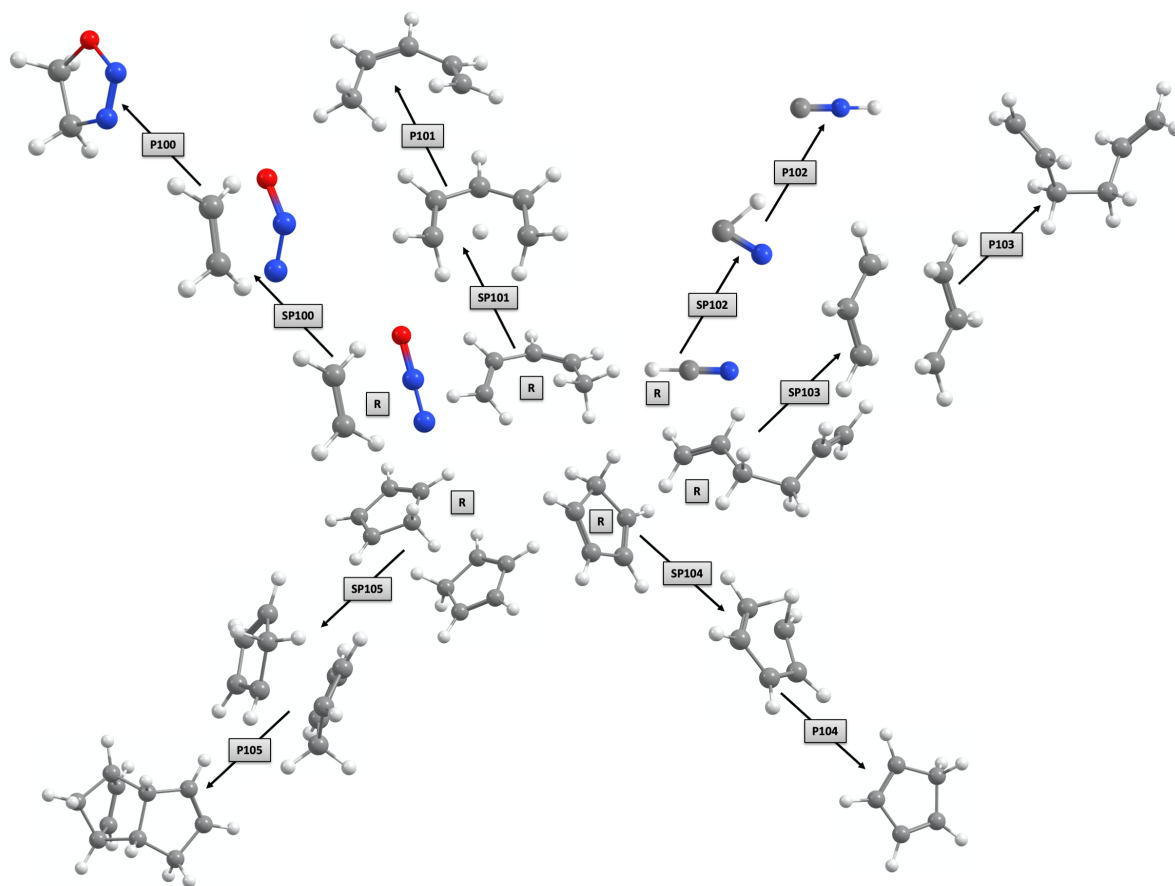


Figure 16: Reactant, saddle point and product configurations for reactions 100–105.

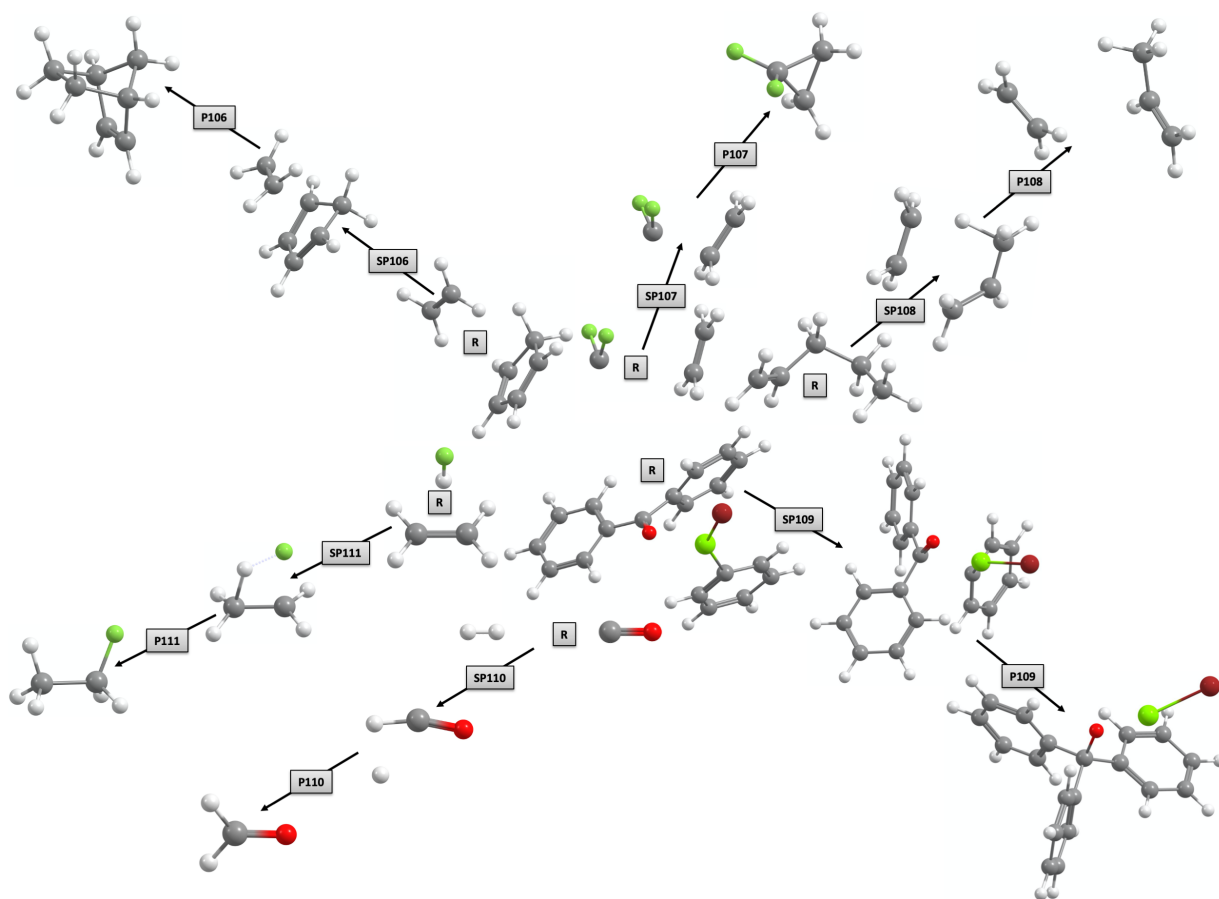


Figure 17: Reactant, saddle point and product configurations for reactions 106–111.

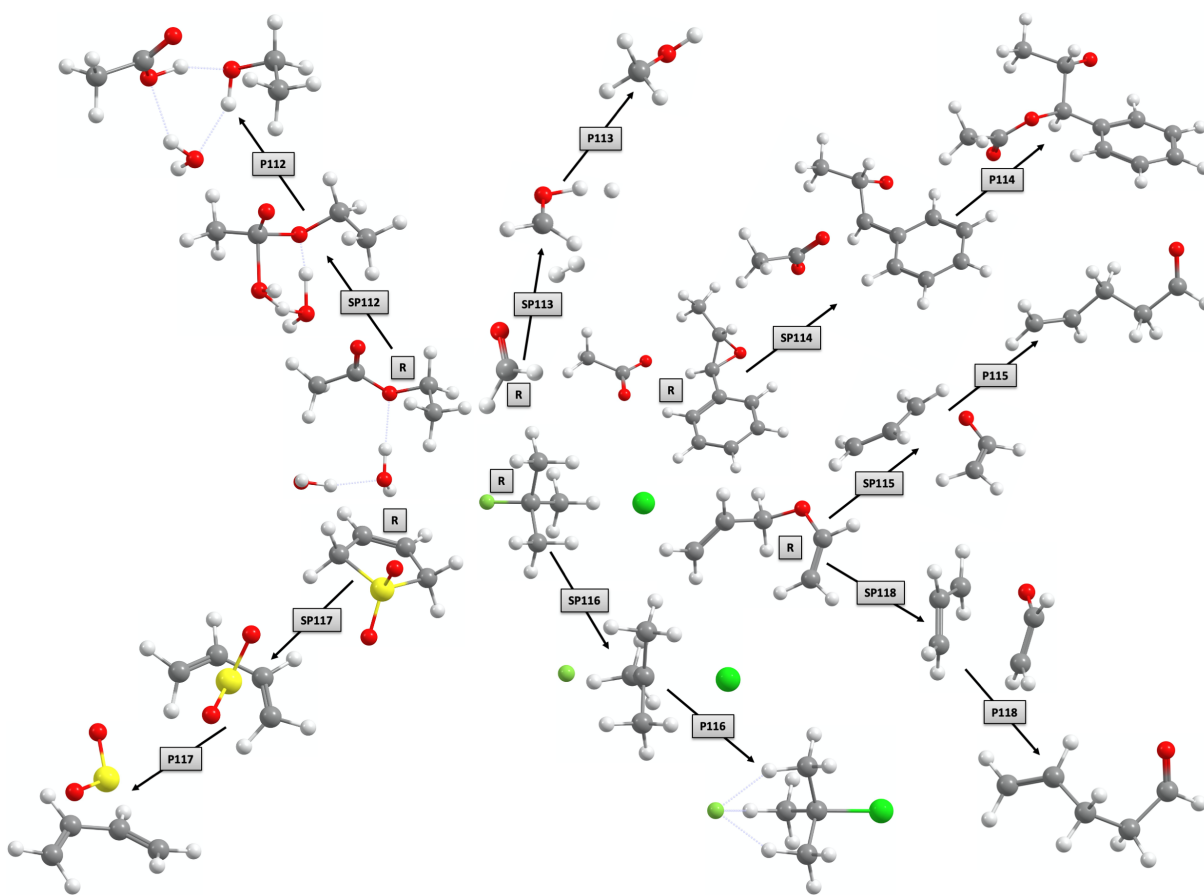
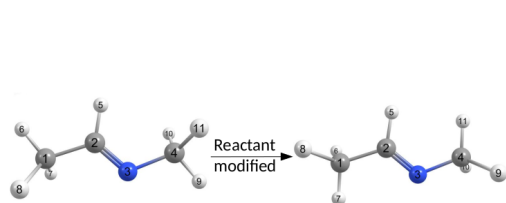
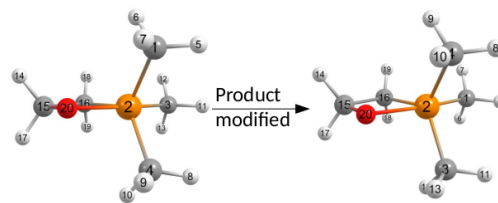


Figure 18: Reactant, saddle point and product configurations for reactions 112–118.

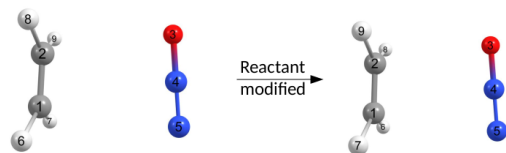
SI-1.2 Modifications of reactant and/or product configurations



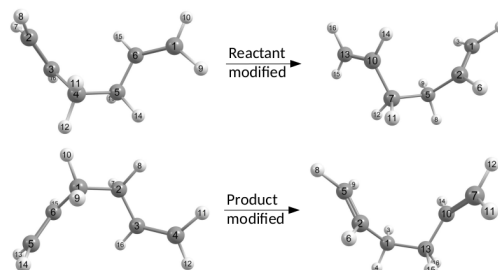
(a) Reaction 58



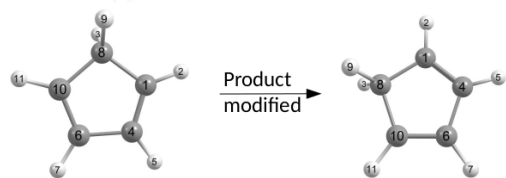
(b) Reaction 82



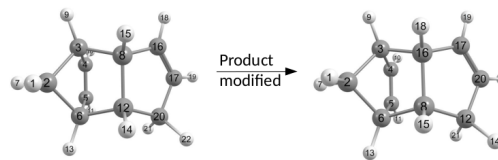
(c) Reaction 100



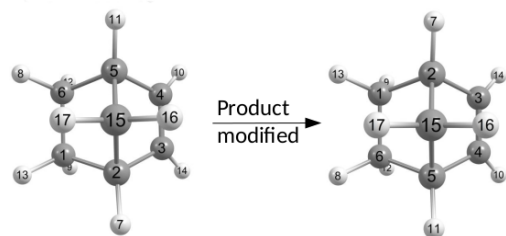
(d) Reaction 103



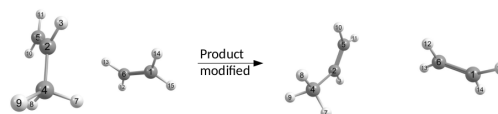
(e) Reaction 104



(f) Reaction 105

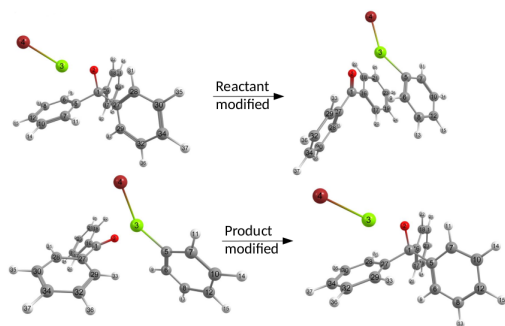


(g) Reaction 106

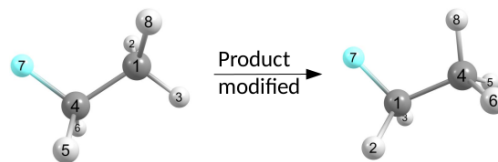


(h) Reaction 108

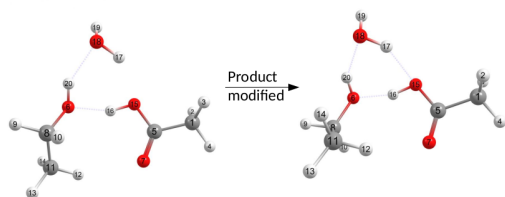
Figure 19: Modifications made to the reactant or product configurations of the original benchmark set of main-group molecular reactions.^{1,2}



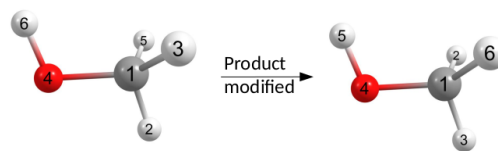
(a) Reaction 109



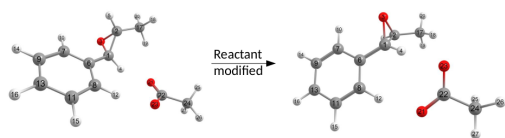
(b) Reaction 111



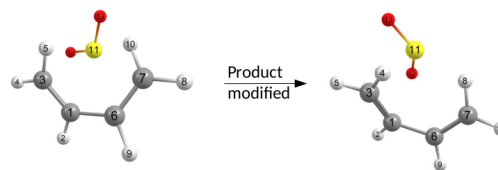
(c) Reaction 112



(d) Reaction 113



(e) Reaction 114



(f) Reaction 117

Figure 20: Modifications made to the reactant or product configurations of the original benchmark set of main-group molecular reactions.^{1,2}

SI-1.3 Energy barrier, reaction energy and imaginary frequency

In this section, the potential energy barrier, reaction energy and imaginary frequency obtained at the first order saddle points are given for the large benchmark set of main-group molecular reactions.

Table 1: Potential energy barrier height, reaction energy and the absolute imaginary frequency at the saddle point for reactions 1–30

Rxn No.	E^\ddagger [kcal/mol]	E_{rxn} [kcal/mol]	$ \omega_0 $ [cm^{-1}]
1	9.2	-6.3	343.5
2	88.2	-6.3	936.9
3	28.6	-4.5	1246.3
4	91.2	0.0	2450.5
5	67.6	0.0	2576.7
6	19.7	0.2	432.5
7	53.8	16.4	1486.6
8	35.9	-11.3	219.3
9	32.4	-2.7	169.1
10	42.1	3.3	1382.9
11	37.0	3.6	1337.6
12	36.6	11.7	217.1
13	32.5	17.9	158.7
14	56.4	-29.1	1217.2
15	50.6	-24.6	1217.5
16	12.2	-23.2	839.3
17	98.3	-19.4	592.6
18	79.4	-18.2	1081.4
19	78.8	-14.5	2144.9
20	67.1	-9.3	723.5
21	38.7	-8.6	1734.7
22	31.1	-1.6	1339.0
23	82.7	0.0	2854.8
24	62.6	3.6	774.6
25	72.1	2.7	1271.0
26	55.5	-12.9	535.5
27	48.5	0.0	506.0
28	37.1	3.6	1557.1
29	68.3	13.0	2139.1
30	120.2	41.4	2023.1

Table 2: Potential energy barrier height, reaction energy and the absolute imaginary frequency at the saddle point for reactions 31–60

Rxn No.	E^\ddagger [kcal/mol]	E_{rxn} [kcal/mol]	$ \omega_0 $ [cm^{-1}]
31	54.6	-25.3	244.9
32	54.1	-25.3	402.1
33	46.8	-20.4	287.7
34	111.0	3.7	1306.7
35	99.4	28.2	1729.4
36	32.2	-9.6	1507.7
37	53.9	-11.4	2110.1
38	83.7	2.8	1541.1
39	82.5	9.3	601.9
40	87.6	17.1	397.8
41	81.6	31.9	1604.1
42	49.7	-16.6	1754.5
43	52.1	-13.3	2097.4
44	66.8	-5.4	2114.1
45	41.7	0.1	2108.7
46	68.4	2.8	1268.7
47	48.7	5.3	1958.0
48	83.9	9.1	1676.4
49	71.1	13.0	543.6
50	100.0	12.1	1471.9
51	67.9	-12.2	643.3
52	34.2	-9.8	1634.6
53	28.5	0.0	1489.4
54	48.1	0.0	1854.2
55	65.7	13.4	1950.7
56	81.1	-13.5	2020.1
57	65.6	5.0	1974.1
58	71.5	15.4	1666.0
59	91.7	33.6	1455.1
60	71.5	33.4	1666.2

Table 3: Potential energy barrier height, reaction energy and the absolute imaginary frequency at the saddle point for reactions 61-90

Rxn No.	E^\ddagger [kcal/mol]	E_{rxn} [kcal/mol]	$ \omega_0 $ [cm^{-1}]
61	46.8	11.8	1337.4
62	82.0	0.0	1290.0
63	82.4	7.7	112.3
64	5.4	-52.6	1133.1
65	54.1	0.5	433.2
66	123.2	20.0	1371.0
67	50.5	-15.4	1997.4
68	31.2	-15.2	519.8
69	15.8	-48.3	516.7
70	56.5	-37.1	727.0
71	91.1	-27.4	1878.0
72	38.2	-25.8	434.4
73	67.5	-23.9	709.4
74	75.3	-21.1	92.0
75	75.0	-20.8	47.7
76	81.5	-18.6	1408.4
77	36.5	-16.5	925.2
78	124.3	0.2	1735.7
79	64.2	8.0	1549.4
80	44.0	9.1	719.1
81	36.5	-16.9	924.3
82	48.4	-11.8	418.8
83	80.7	-11.6	889.5
84	52.5	-0.6	1596.4
85	35.2	0.2	392.1
86	52.5	4.4	505.7
87	48.9	0.8	525.0
88	6.3	0.2	44.8
89	2.7	0.6	68.6
90	87.5	4.3	442.9

Table 4: Potential energy barrier height, reaction energy and the absolute imaginary frequency at the saddle point for reactions 91-121

Rxn No.	E^\ddagger [kcal/mol]	E_{rxn} [kcal/mol]	$ \omega_0 $ [cm^{-1}]
91	84.6	3.9	778.8
92	75.1	4.0	571.5
93	53.1	0.1	558.7
94	73.5	8.2	1758.9
95	98.5	14.5	1387.3
96	17.1	-59.1	424.5
97	48.3	1.7	667.1
98	29.0	2.4	2132.7
99	28.1	-0.6	2127.8
100	25.6	-5.3	466.8
101	32.9	0.0	1549.5
102	47.8	13.6	1116.6
103	32.6	0.2	526.5
104	26.6	0.0	1194.2
105	15.2	-19.1	440.8
106	17.1	-25.6	488.4
107	8.8	-53.9	405.7
108	55.5	25.9	1156.6
109	18.3	-12.8	205.0
110	74.0	-10.4	1880.6
111	44.1	-16.1	1845.9
112	35.5	-5.3	1264.4
113	75.9	-25.1	1385.4
114	21.6	11.1	304.7
115	62.8	-18.0	401.3
116	45.4	29.5	391.1
117	18.9	2.4	348.2
118	31.6	-18.3	434.1
119	2.4	-4.1	861.0
120	52.6	0.0	1492.0
121	39.0	-4.1	916.4

SI-2 Data relevant to the (EW-)CI-NEB method

SI-2.1 Comparison of linear interpolation in Cartesian coordinates and the IDPP method

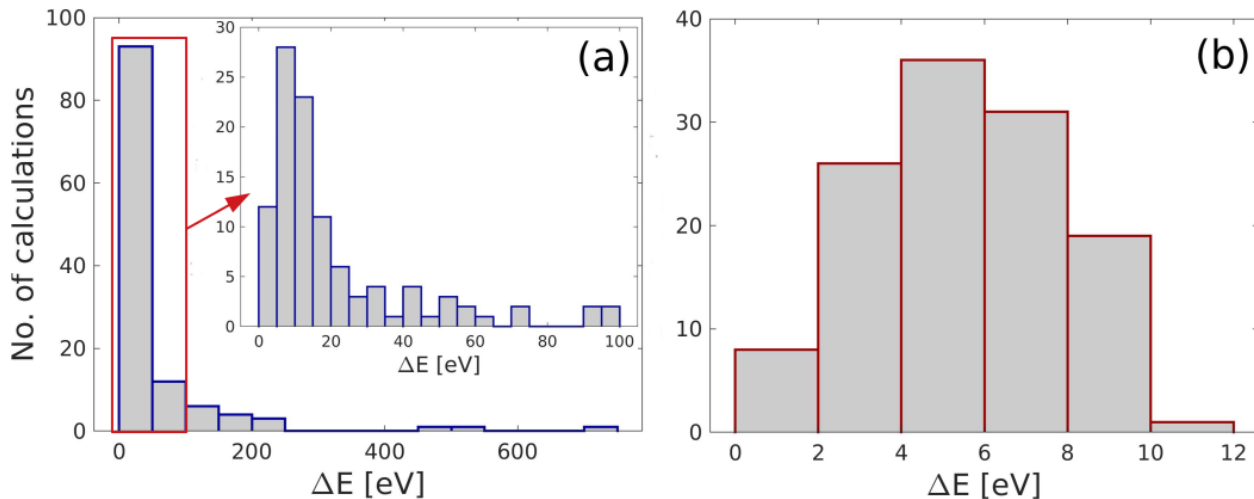


Figure 21: The maximum rise in energy ($\Delta E = E^{\text{HEI}} - E^{\text{reactant}}$) along initial paths generated by linear interpolation in Cartesian coordinates (shown in (a)) and by the IDPP method (shown in (b)) for the large benchmark set of main-group molecular reactions. For clarity the distribution of $\Delta E \in (0, 100]$ kcal/mol is shown as an inset in (a).

SI-2.2 Path lengths obtained by (EW-)CI-NEB

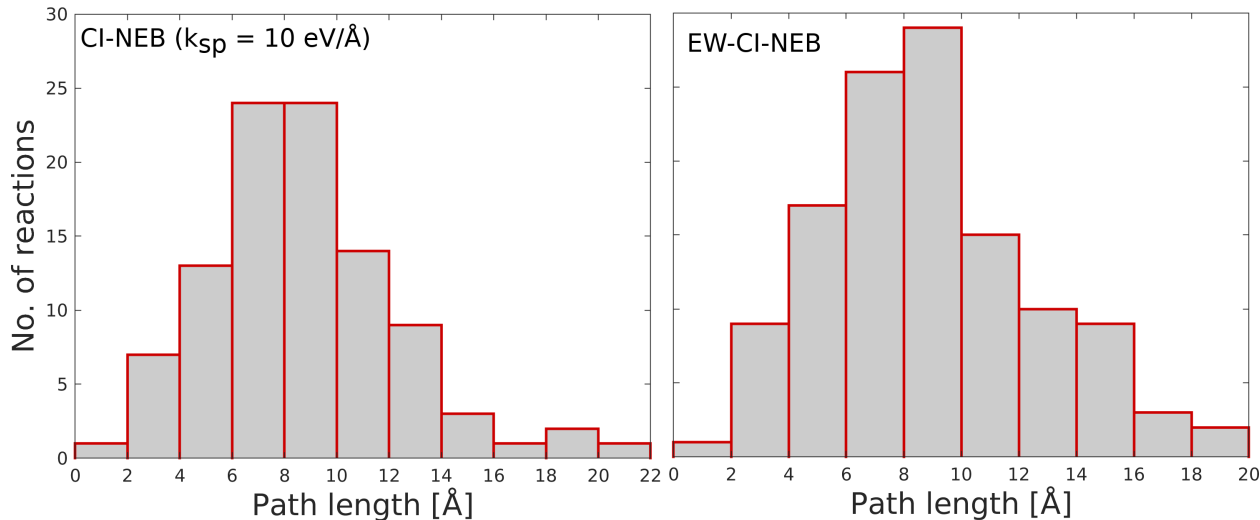


Figure 22: Distribution of path lengths of converged CI-NEB and EW-CI-NEB calculations, using $N_{\text{im}} = 10$.

SI-2.3 Evolution of inter-image distance in (EW-)CI-NEB

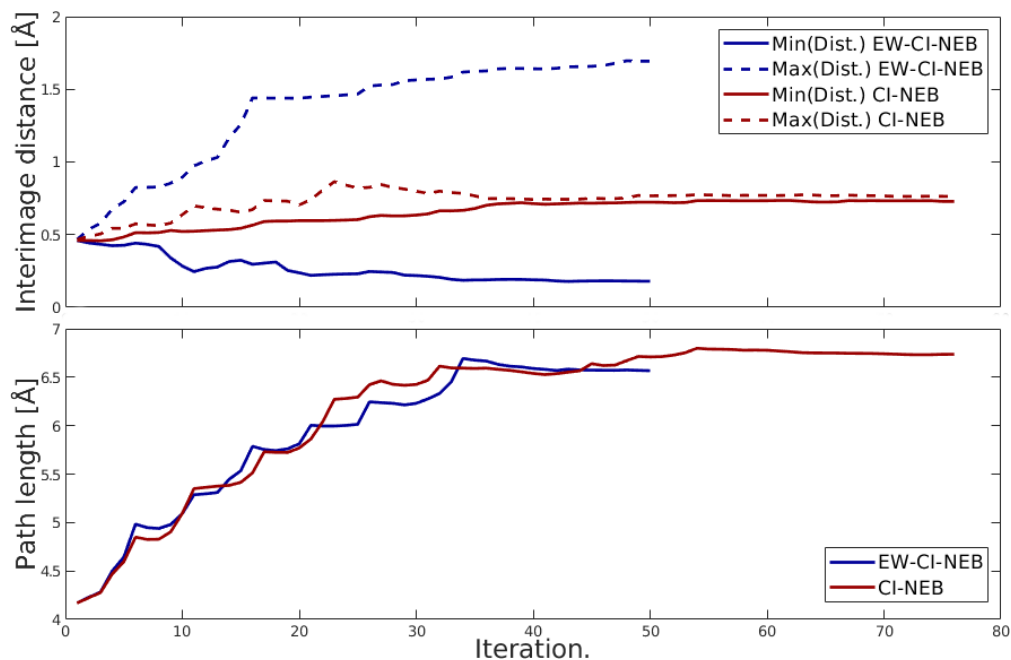


Figure 23: Features of the reaction path in CI-NEB and EW-CI-NEB calculations on the ene-reaction of 1-propylene and ethylene. In the upper panel, the evolution of the maximum and minimum inter-image distance along the reaction path during the CI-NEB (red) and EW-CI-NEB (blue) optimization. In the lower panel, the evolution of the path length. The calculations are started from an IDPP initial path.

SI-2.4 Inter-image distances and angle distribution in (EW-)CI-NEB

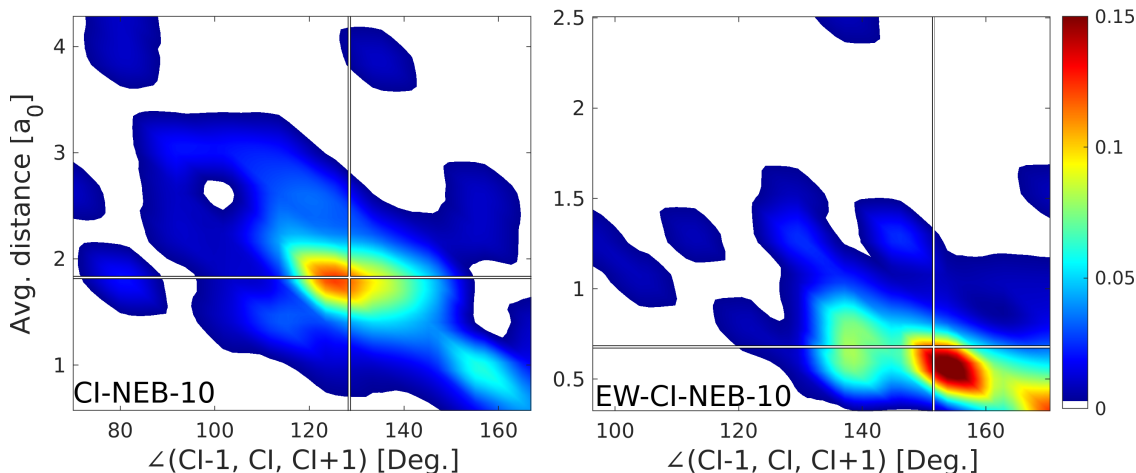


Figure 24: Bivariate distribution of average inter-image distances of CI to its two neighboring images and the angle formed by the three images along the converged path for CI-NEB and EW-CI-NEB calculations on the large benchmark set of main-group molecular reactions.

To further investigate the image distribution along the reaction paths obtained by CI-NEB and EW-CI-NEB calculations on the large benchmark set of main-group molecular reactions, the deviation from 'ideality' is computed. For this purpose, the reaction is partitioned into two segments, to the left and right of CI. The deviation from the ideal even distribution is then computed,

$$\gamma_{\text{left}} = \frac{|\mathbf{R}_{\text{CI}} - \mathbf{R}_{\text{CI-1}}|}{\sum_{i=0}^{\text{CI-1}} |\mathbf{R}_{i+1} - \mathbf{R}_i|}$$

$$\gamma_{\text{right}} = \frac{|\mathbf{R}_{\text{CI+1}} - \mathbf{R}_{\text{CI}}|}{\sum_{i=\text{CI}}^N |\mathbf{R}_{i+1} - \mathbf{R}_i|}$$

Then, γ is selected as the interval that exhibits a larger deviation from an even distribution (i.e., $\gamma = 1.0$). The results are shown in Fig. 25.

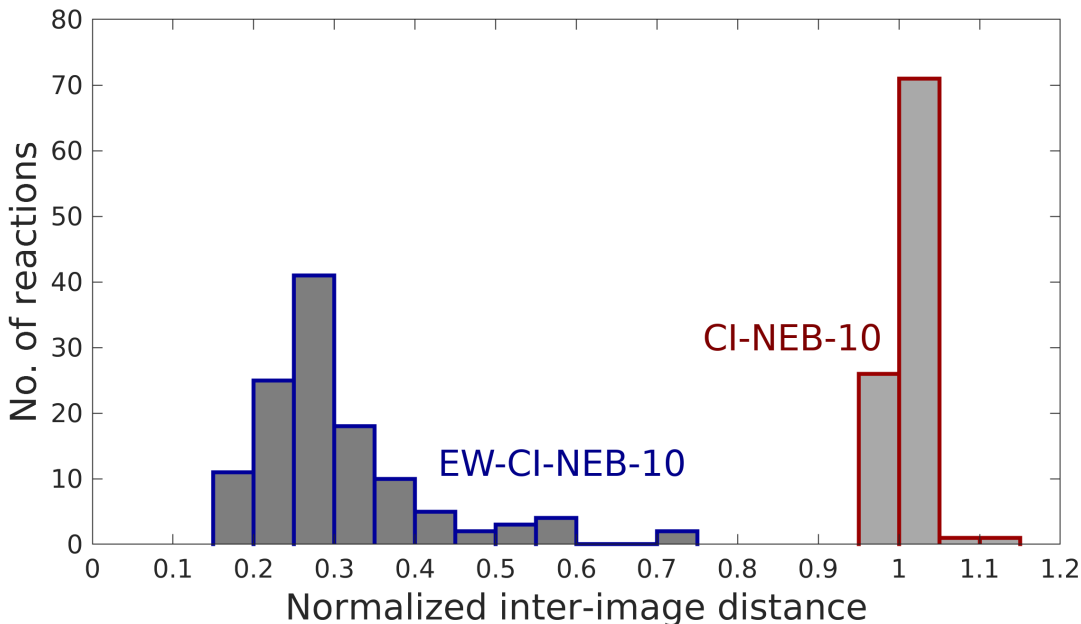


Figure 25: The deviation of the inter-image distance of CI to its neighboring images from an ideal even distribution along the reaction path. The results are shown for CI-NEB and EW-CI-NEB calculations on the large benchmark set of molecular reactions.

SI-2.5 Optimization profile to monitor (EW-)CI-NEB calculations

In this study, we present a new tool to visualize and monitor (EW-)CI-NEB calculations and call it an optimization profile. In this scheme, the path at every optimization step is interpolated using a piecewise-cubic polynomial³ and plotted along with the position of the intermediate images. This allows us to visualize how the path/images 'slide down' on the energy surface towards the MEP. Optimization profiles may also reveal whether the path may be kinked, calculation may become nonconvergent or if the optimization has become unstable. Furthermore, an optimization profile will also reveal whether an intermediate energy minima is to be found along the path. In such cases, it may be the best choice of action to halt the calculation, locate the intermediate energy minimum and carry out CI-NEB calculation for the two path fragments, i.e. from reactant to intermediate state and from intermediate to product state. The tool to generate an optimization profile from a NEB calculation in ORCA is available in Ref.⁴

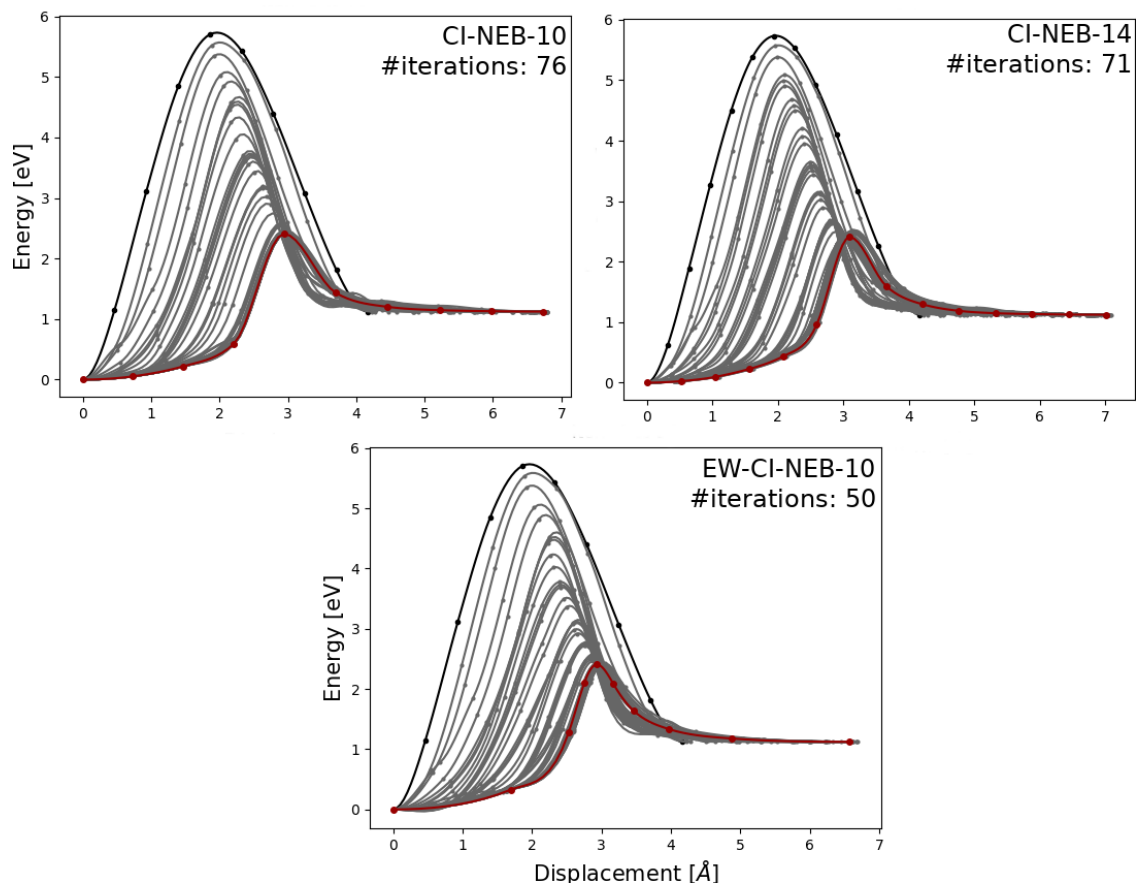


Figure 26: Optimization profiles for CI-NEB and EW-CI-NEB calculations using $N_{\text{im}} = 10$ and 14 of the ene-reaction of 1-propylene and ethylene.

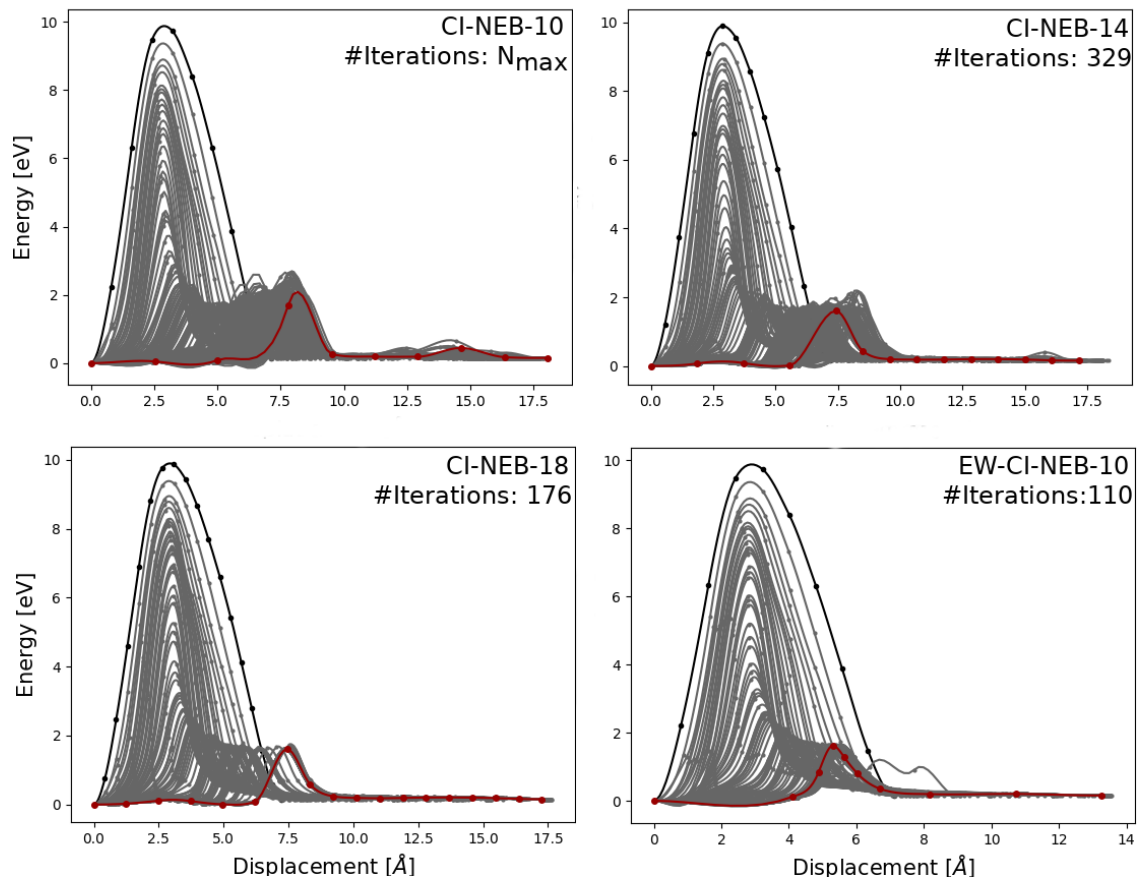


Figure 27: CI-NEB and EW-CI-NEB optimization profiles for the reaction $BH_3NH_3 + BH_2NH_2 \rightarrow 2BH_2NH_2 + H_2$ using $N_{im} = 10, 14$ and 18 .

SI-2.6 Convergence behavior of CI and TS

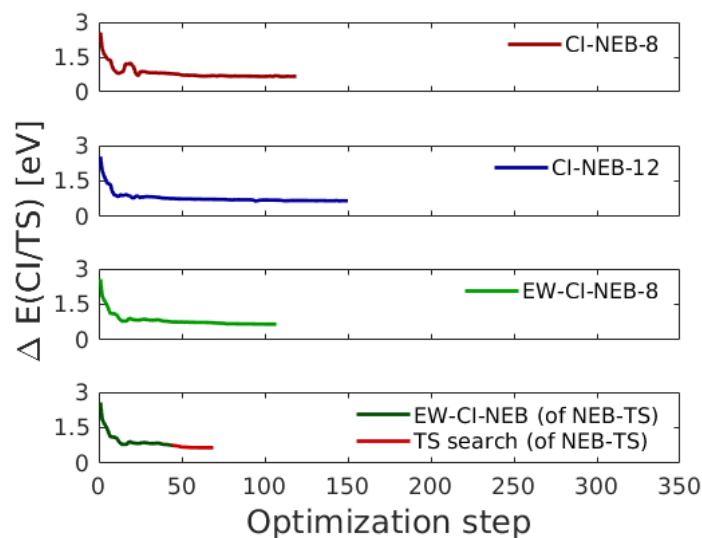


Figure 28: The relative energy of CI and TS as a function of optimization step for CI-NEB, EW-CI-NEB and NEB-TS calculations, using both $N_{\text{im}} = 8$ and 12, of the Diels-Alder addition of two cyclopentadienes.

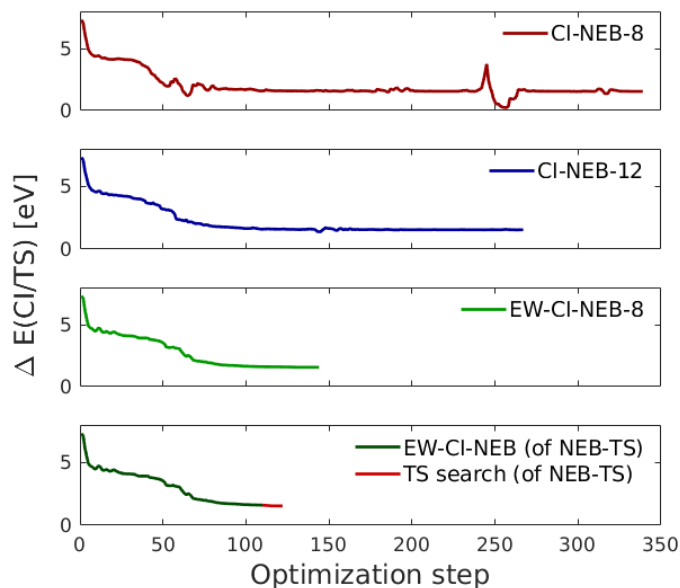


Figure 29: The relative energy of CI and TS as a function of optimization steps for CI-NEB, EW-CI-NEB and NEB-TS calculations, using both $N_{\text{im}} = 8$ and 12, of the hydrolysis reaction of ethyl acetate.

SI-3 Additional data for NEB-TS and IDPP-TS methods

SI-3.1 Energy deviation of NEB-TS (and IDPP-TS) saddle points from reference set of saddle points

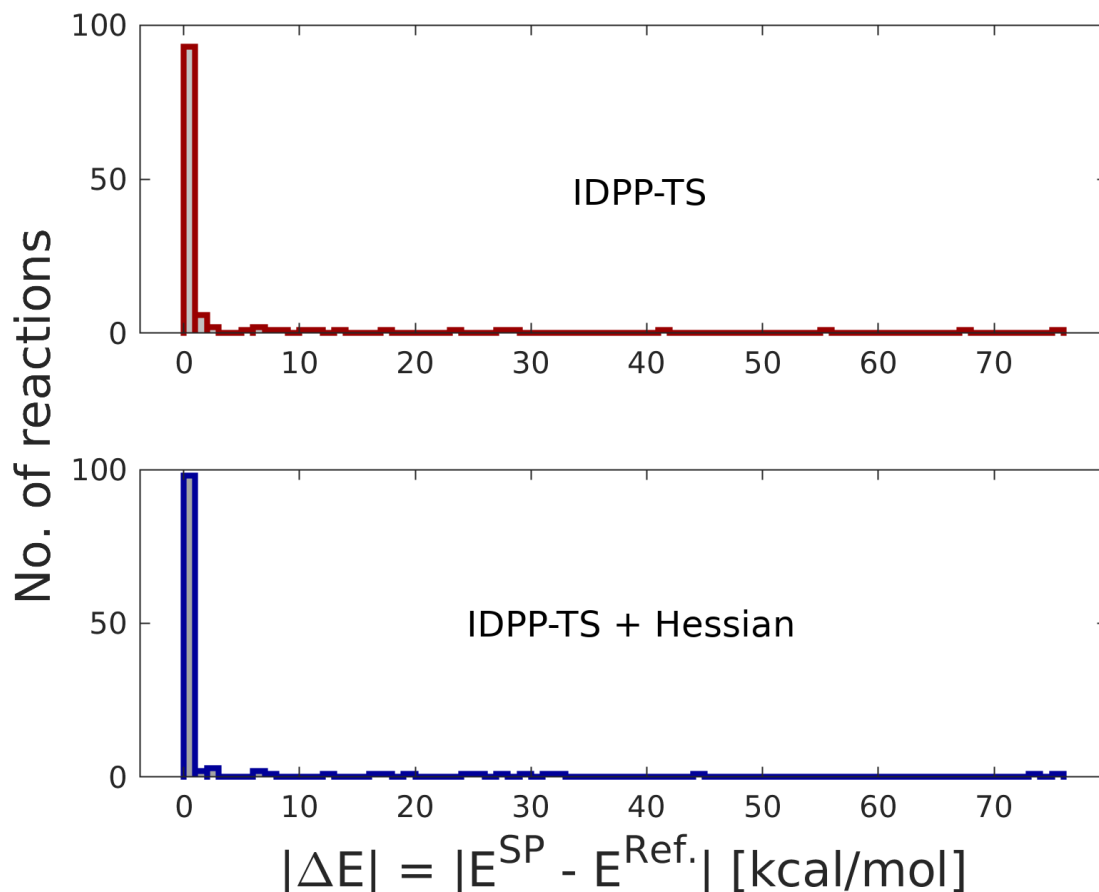


Figure 30: Energy deviation of saddle points obtained by IDPP-TS from the reference set of saddle points. In the upper panel, the TS search is started using a modified empirical Hessian matrix. In the lower panel, the TS search is started using the exact Hessian matrix. In both sets of calculations, the initial configuration of the TS search is taken as the highest energy image along an IDPP initial path.

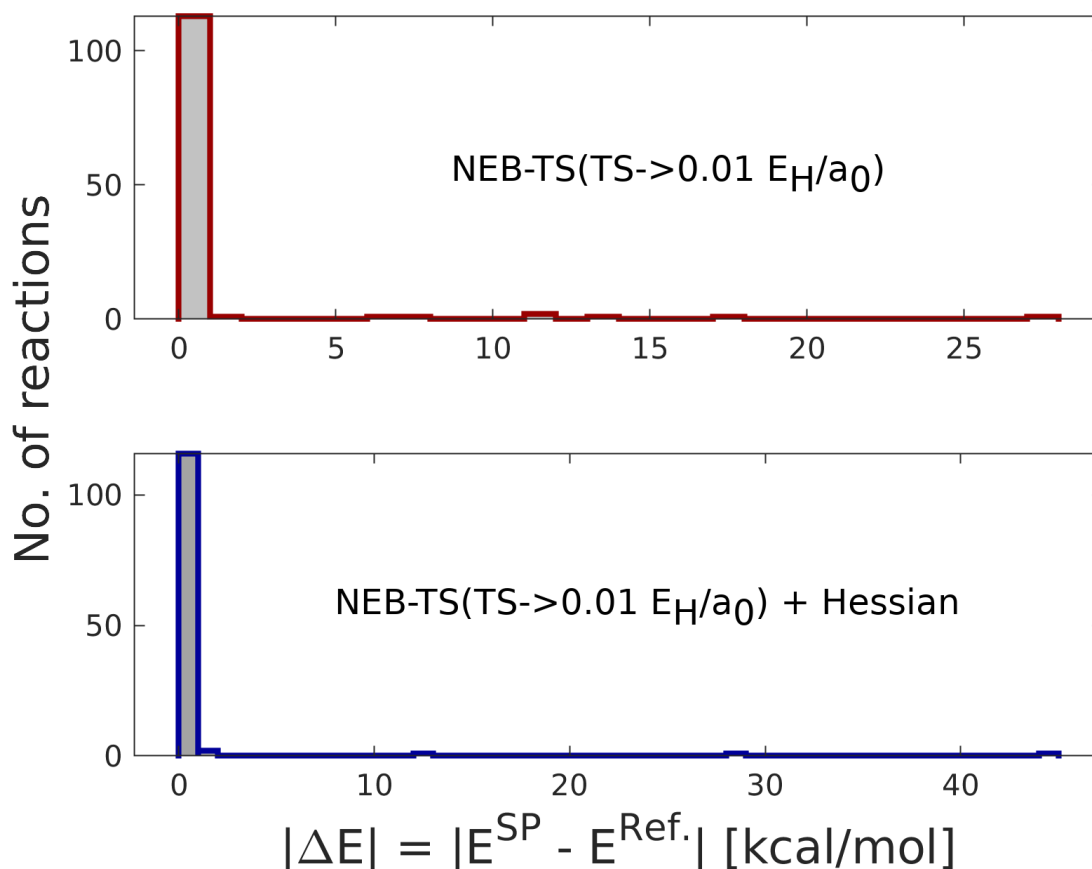


Figure 31: Energy deviation of saddle points obtained by NEB-TS from the reference set of saddle points. The NEB-TS calculations use a TS activation threshold of $\epsilon_{max}^{TS} = 0.01 E_H/a_0$. In the upper panel, the TS search is started using a modified empirical Hessian matrix. In the lower panel, the TS search is started using the exact Hessian matrix. In both sets of calculations, the initial configuration of the TS search is taken as the climbing image from a partially converged EW-CI-NEB calculation.

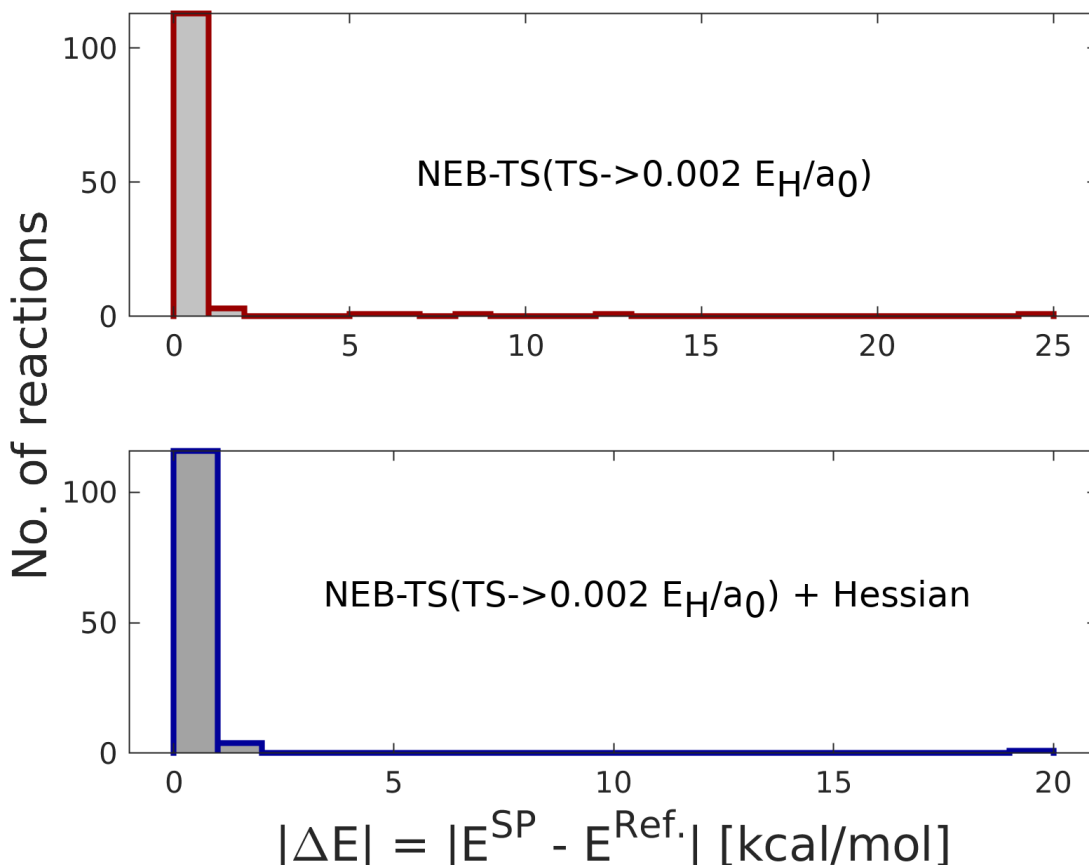


Figure 32: Energy deviation of saddle points obtained by NEB-TS from the reference set of saddle points. The NEB-TS calculations use a TS activation threshold of $\epsilon_{max}^{\text{TS}} = 0.002 E_H/a_0$. In the upper panel, the TS search is started using a modified empirical Hessian matrix. In the lower panel, the TS search is started using the exact Hessian matrix. In both sets of calculations, the initial configuration of the TS search is taken as the climbing image from a partially converged EW-CI-NEB calculation.

SI-3.2 Further analysis of selected reactions

SI-3.2.1 NEB-TS converges to incorrect saddle point

The NEB-TS method can converge to an incorrect saddle point, if not executed carefully, i.e. a saddle point that is not connected to the given reactant or product state. In the following, an example of one such reaction is taken. The reaction of 2-butanol and H₂O to form acetoin. The results of EW-CI-NEB and NEB-TS calculations for this reaction are summarized in Table 5 and Fig. 33.

Table 5: Investigation of the character of the saddle points obtained from NEB-TS calculations on the formation of acetoin from 2-butanol and H₂O. The table shows results from both EW-CI-NEB and NEB-TS calculations, i.e. an estimate of the activation energy E^\ddagger and the absolute value of the imaginary frequency ω_0^\ddagger at the first order saddle point obtained by the calculations. All calculations use $N_{\text{im}} = 10$. The two sets of NEB-TS calculations are carried out using $\epsilon_{\text{max}}^{\text{TS}} \approx 0.1$ and 0.5 eV/Å.

Method	E^\ddagger [eV]	ω_0^\ddagger [cm ⁻¹]
EW-CI-NEB	4.34	1464.5
NEB-TS(≈ 0.1 eV/Å)	4.34	1445.8
NEB-TS(≈ 0.5 eV/Å)	3.83	539.3

The saddle point obtained by EW-CI-NEB and NEB-TS($\epsilon_{\text{max}}^{\text{TS}} \approx 0.1$ eV/Å) are in agreement. This saddle point is denoted as (denoted by SP-I in Fig. 33). The saddle point obtained by NEB-TS($\epsilon_{\text{max}}^{\text{TS}} \approx 0.5$ eV/Å), labeled as SP-II, is approximately 0.51 eV lower in energy than SP-I. Internal reaction coordinate analysis reveals that SP-II is indeed not connected to the given reactant state. The correct saddle point, SP-I, can hence be obtained by lowering the TS activation threshold. Also, sometimes, it may suffice to use a more accurate initial Hessian, than the Almlöf model Hessian matrix used in these NEB-TS calculations. For this particular case, however, NEB-TS($\epsilon_{\text{max}}^{\text{TS}} \approx 0.5$ eV/Å) using an exact Hessian also converges to SP-II.

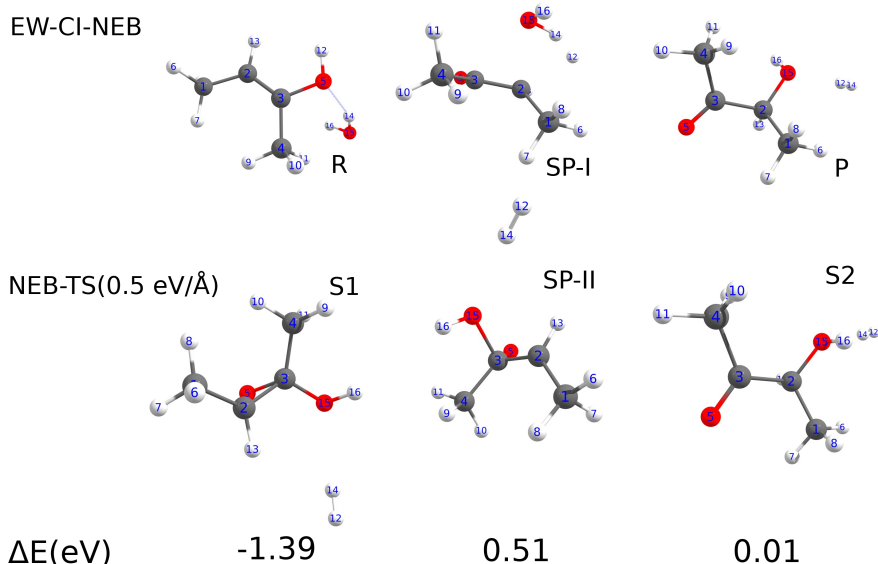


Figure 33: Internal reaction coordinate analysis of saddle points obtained by NEB-TS calculations carried out on the reaction of 2-butanol and H_2O to form acetoin. The reactant, product and correct saddle point (SP-I) configurations are shown in the upper panel. The configuration of the incorrect saddle point (SP-II), obtained by a NEB-TS ($\approx 0.5 \text{ eV}/\text{\AA}$) calculation, is shown in the center of the lower panel. From an internal reaction coordinate analysis started on SP-II, two energy minima are obtained, labeled as S1 and S2. The configuration of these energy minima is shown in the lower panel. ΔE is the energy difference between the configurations of the upper and lower panel.

SI-3.2.2 An alternative saddle point obtained by NEB-TS

The NEB-TS method can converge to saddle points that belong to a different reaction path connecting the same given reactant and product states. In the following, an example of one such reaction is taken. The cyclization of propene to form cyclopropane. The results of EW-CI-NEB and NEB-TS calculations for this reaction are summarized in Table. 6 and Figs. 34, 35 and 36. As is evident, the cyclization reaction is a very challenging reaction path that is characterized by an extremely flat and high energy barrier, see Fig. 34.

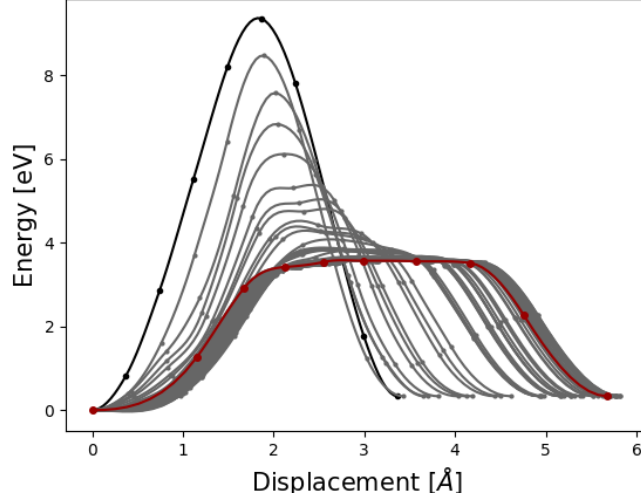


Figure 34: Optimization profile for a EW-CI-NEB-10 calculation the cyclization reaction of propene.

The EW-CI-NEB method converges to a saddle point (SP-I) that gives an activation energy of $E^\ddagger = 4.34$ in agreement to the saddle point obtained by NEB-TS($\epsilon_{\text{max}}^{\text{TS}} \approx 0.5$). Note the geometries are also nearly the same. However, the magnitude of the vibrational frequency calculated from the two saddle points is 74.0 and 330.9 cm^{-1} . While, the saddle point (SP-II) obtained by NEB-TS($\epsilon_{\text{max}}^{\text{TS}} \approx 0.1$), is roughly 0.25 eV higher in energy than that of EW-CI-NEB.

Table 6: Investigation of the character of the saddle points obtained from NEB-TS calculations on the cyclization reaction of propene. The table shows results from both EW-CI-NEB and NEB-TS calculations, i.e. an estimate of the activation energy E^\ddagger and the absolute value of the imaginary frequency ω_0^\ddagger at the first order saddle point obtained by the calculations. All calculations use $N_{\text{im}} = 10$. The two sets of NEB-TS calculations are carried out using $\epsilon_{\text{max}}^{\text{TS}} \approx 0.1$ and 0.5 eV/\AA .

Method	E^\ddagger [eV]	$ \omega_0^\ddagger $ [cm^{-1}]
EW-CI-NEB	3.57	74.0
NEB-TS($\approx 0.1 \text{ eV/\AA}$)	3.82	574.1
NEB-TS($\approx 0.5 \text{ eV/\AA}$)	3.59	330.9

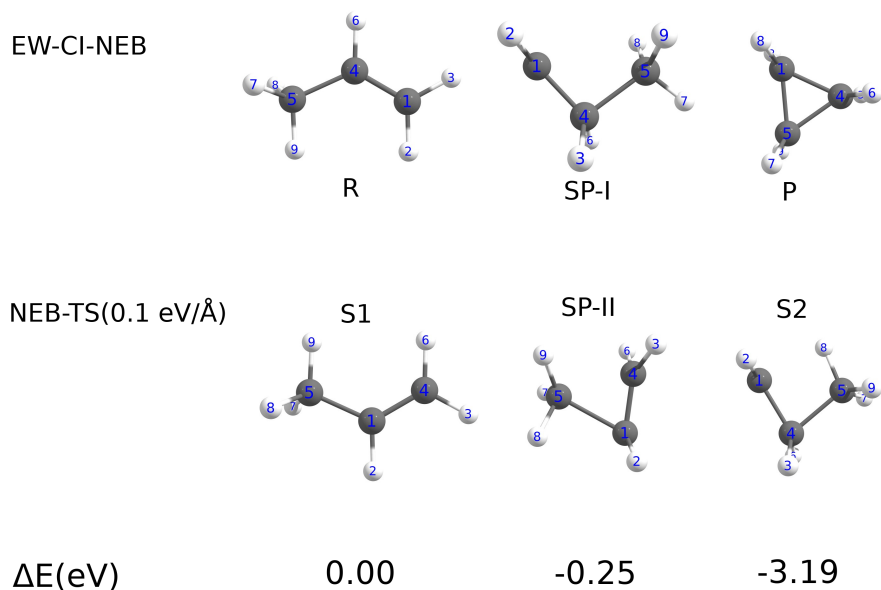


Figure 35: Internal reaction coordinate analysis of saddle points obtained by NEB-TS calculations carried out on the reaction of cyclization reaction of propene. The reactant, product and correct saddle point (SP-I) configurations are shown in the upper panel. The configuration of the other saddle point (SP-II), obtained by a NEB-TS(≈ 0.1 eV/Å) calculation, is shown in the center of the lower panel. From an internal reaction coordinate analysis started on SP-II, two energy minima are obtained, labeled as S1 and S2. The S1 corresponds to the given reactant energy minimum, while S2 corresponds to some very shallow intermediate configuration on the flat surface along the top of the energy barrier. The configuration of these energy minima is shown in the lower panel. ΔE is the energy difference between the configurations of the upper and lower panel.

IRC analysis from SP-II reveals that this saddle point is connected to the reactant state. However, the second state obtained by the IRC calculations is a very shallow intermediate energy minimum located on the top of the flat energy barrier. Therefore, to further investigate the connectivity of SP-II, two EW-CI-NEB calculations are carried out. Namely, from the reactant state to SP-II and from SP-II to the product state. The results are summarized in Fig. 36.

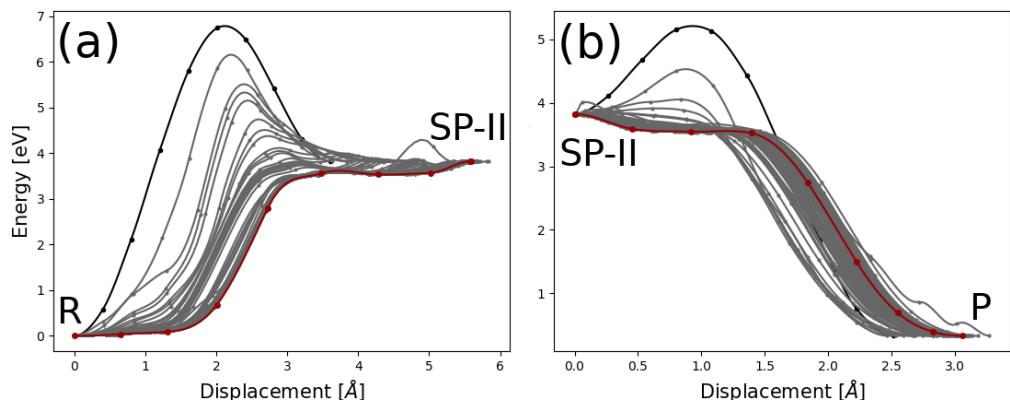


Figure 36: Optimization profile for two EW-CI-NEB-10 calculations on the cyclization reaction of propene. The calculations are started from an initial path constructed using the reactant state and SP-II (left) and from SP-II to the product state (right). SP-II is the saddle point obtained by the NEB-TS($\epsilon_{\text{max}}^{\text{TS}} \approx 0.1 \text{ eV/\AA}$) calculations. The EW-CI-NEB calculations indicate that SP-II is indeed connected to the same reactant and product states as SP-I, i.e. the SP obtained by the NEB-TS($\epsilon_{\text{max}}^{\text{TS}} \approx 0.1 \text{ eV/\AA}$) calculation.

The two partitioned EW-CI-NEB calculations carried out indicate that SP-II is likely to be connected to the given reactant and product energy minima, i.e. if the very shallow intermediate energy minimum along the path is excluded. Therefore, to conclude, it is highly likely that the NEB-TS($\epsilon_{\text{max}}^{\text{TS}} \approx 0.1 \text{ eV/\AA}$) calculation identifies a saddle point that characterizes an alternative reaction coordinate than the one obtained by EW-CI-NEB and NEB-TS($\epsilon_{\text{max}}^{\text{TS}} \approx 0.5 \text{ eV/\AA}$) calculations. Interestingly, if the exact Hessian is used as the initial Hessian matrix in NEB-TS($\epsilon_{\text{max}}^{\text{TS}} \approx 0.1 \text{ eV/\AA}$) the calculation converges to SP-I.

SI-3.2.3 NEB-TS identifies different saddle point on same path

The NEB-TS method can converge to a different saddle point (than the highest energy one) along a multiple extrema reaction path. In the following, an example of one such reaction is taken. The rearrangement of allyl-phenyl-ether to phenylpropylene oxide. The results of EW-CI-NEB and NEB-TS calculations for this reaction are summarized in Table 7 and Figs. 37 and 38. This reaction is (at least) a two-step reaction pathway. Therefore, by locating the intermediate energy minimum and carrying out two EW-CI-NEB calculations, i.e., from the reactant to intermediate state and from the intermediate to the product state, the two saddle points along the reaction coordinate are obtained accurately, see Fig. 37.

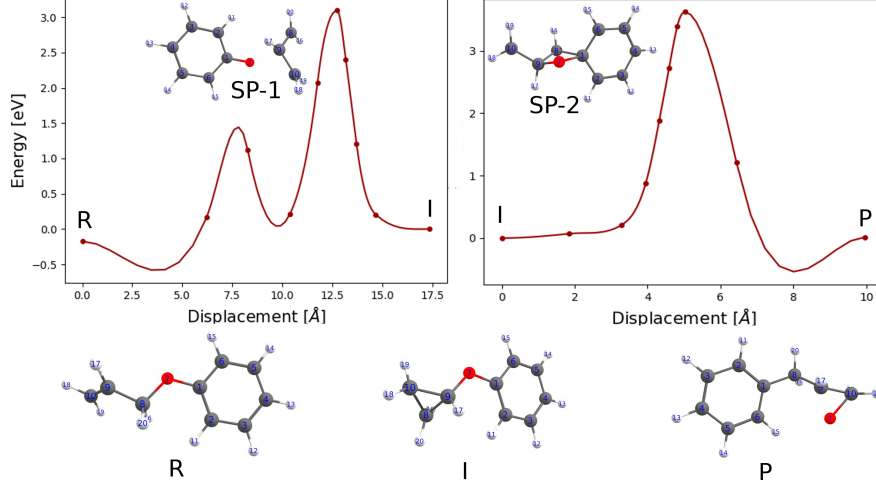


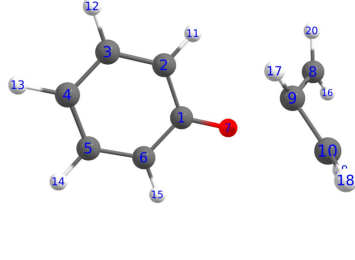
Figure 37: Energy profiles for the rearrangement of allyl-phenyl-ether to phenylpropylene. The reaction coordinate includes an intermediate energy minimum (labeled as I) and hence two EW-CI-NEB calculations are carried out, from the reactant (R) to the intermediate state and from the intermediate to the product state (P). The two saddle points along the coordinate are labeled as SP-1 and SP-2. The reactant, product, and intermediate state configurations along with the two saddle point configurations are shown as insets. The EW-CI-NEB calculations are considered converged when the atom forces acting on CI drop below the prescribed convergence thresholds. Therefore, the initial energy maximum, at around $x = 7.5$ Å, is not necessarily a true energy maximum along the reaction path (and hence a first order saddle point on the energy surface). It could be only an artefact of the interpolation, as the atom forces acting tangential to the path are used by the interpolant.

The saddle point included in the reference set of saddle points is SP-2 and corresponds to the highest energy, first order, saddle point along the reaction path. While, the saddle points obtained by NEB-TS($\epsilon_{\max}^{\text{TS}} \approx 0.5$) eV/Å and NEB-TS($\epsilon_{\max}^{\text{TS}} \approx 0.1$) eV/Å correspond to SP-1, see Fig. 38. If the exact Hessian is used as the initial Hessian matrix, the two NEB-TS calculations converge to the higher energy saddle point, i.e. SP-2.

Table 7: Investigation of the character of the saddle points obtained from NEB-TS calculations on the rearrangement of allyl-phenyl-ether to phenylpropylene oxide. The table shows results from two intermediate EW-CI-NEB calculations and NEB-TS calculations, i.e. an estimate of the activation energy E^\ddagger and the absolute value of the imaginary frequency ω_0^\ddagger at the first order saddle point obtained by the calculations. All calculations use $N_{\text{im}} = 10$. The two sets of NEB-TS calculations are carried out using $\epsilon_{\max}^{\text{TS}} \approx 0.1$ and 0.5 eV/Å.

Method	E^\ddagger [eV]	$ \omega_0^\ddagger $ [cm^{-1}]
EW-CI-NEB (SP-1)	3.79	442.0
EW-CI-NEB (SP-2)	3.27	561.2
NEB-TS(≈ 0.1 eV/Å)	3.26	568.2
NEB-TS(≈ 0.5 eV/Å)	3.28	557.6 (note that $\omega_1 = -34.0$)

SP from NEB-TS(0.1 eV/Å)



SP from NEB-TS(0.5 eV/Å)

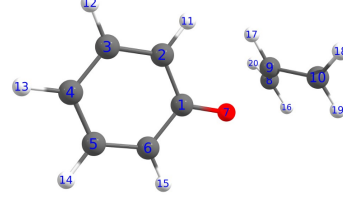


Figure 38: Saddle point configurations obtained from NEB-TS using $\epsilon_{\max}^{\text{TS}} \approx 0.1$ and 0.5 eV/Å are shown and are in agreement to SP-1 shown in Fig. 37.

SI-3.3 Vibrational analysis of allyl-vinyl-ether reaction

Table 8: Imaginary frequencies ($\omega_0, \omega_1, \omega_2$) for the NEB-TS calculations of the rearrangement of allyl-vinyl-ether to 1-pentene-5-one, where the TS activation threshold ($\epsilon_{\max}^{\text{TS}}$) is varied. Note that $\epsilon_{\text{RMS}}^{\text{TS}} = \frac{1}{2}\epsilon_{\max}^{\text{TS}}$ in all calculations.

$\epsilon_{\max}^{\text{TS}}$ [E _H /a ₀]	ω_0 [cm ⁻¹]	ω_1 [cm ⁻¹]	ω_2 [cm ⁻¹]
0.02	-488.5	-158.4	-23.0
0.018	-478.9	-151.7	-25.5
0.016	-426.9	-139.0	-38.2
0.014	-426.9	-139.0	-38.2
0.012	-291.4	-165.0	—
0.010	-295.6	-158.6	—
0.008	-295.6	-158.6	—
0.006	-462.6	—	—
0.004	-473.9	—	—
0.002	-466.4	—	—

SI-4 CI-NEB and NEB-TS method parameters

To investigate selected CI-NEB and NEB-TS method parameters, a smaller benchmark set of 5 relatively simple reactions is used. The set includes HCN isomerization (**system 1**), rearrangement reaction of 1,5 hexadiene (**system 2**), Diels-alder cycloaddition (**system 3**), Ene-reaction of 1-propylene and ethylene (**system 4**) and addition of H₂ to formaldehyde (**system 5**).

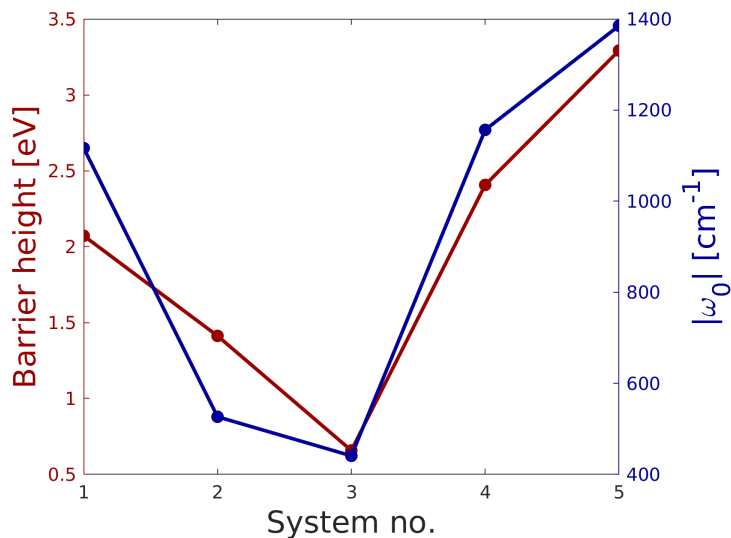


Figure 39: Barrier heights for the five reactions of the small benchmark set are shown by red (left vertical axis). Absolute imaginary frequencies (obtained from the analytical Hessian matrix computed at the saddle points) are shown by blue (right vertical axis).

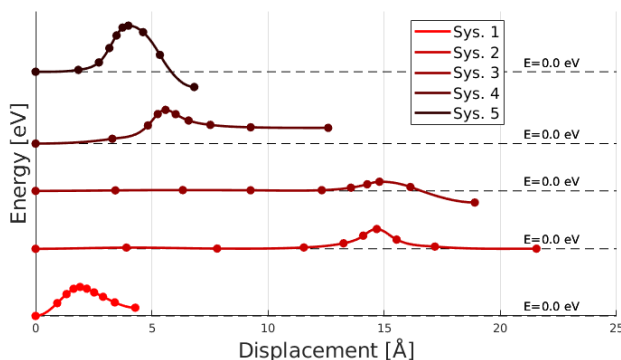


Figure 40: Minimum energy paths for the five reactions of the small benchmark set.

SI-4.1 Effect of the spring constant value

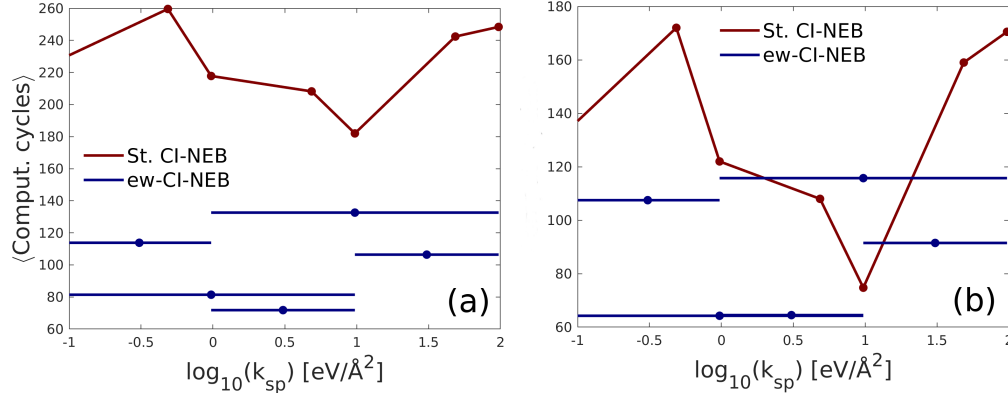


Figure 41: The average number of computational cycles required to complete the small benchmark set using both CI-NEB and EW-CI-NEB as a function of the logarithm of the spring constant, k^{sp} . Note that CI-NEB is unable to converge for system 2. In (a) system 2 is included in the average number of computational cycles, while in (b) it is excluded.

SI-4.2 Effect of the number of images

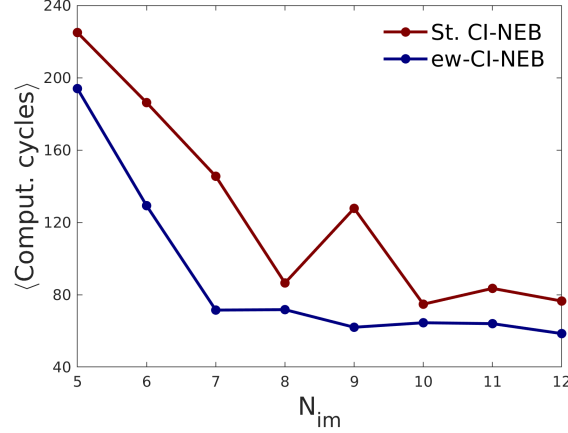


Figure 42: Computational efficiency of CI-NEB (red) and EW-CI-NEB (blue) on the small benchmark set, using variable number of images. Since, CI-NEB calculation of system 2 is nonconvergent. The data from CI-NEB and EW-CI-NEB calculations on system 2 are omitted.

SI-4.3 Comparison: L-BFGS and VPO

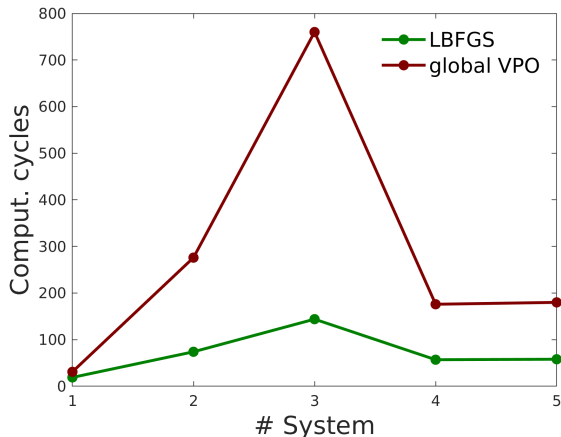


Figure 43: Computational efficiency of EW-CI-NEB calculations measured on the small benchmark set, using both L-BFGS and velocity projection optimization (VPO) method. Note that the total number of optimization steps allowed was increased from 500 to 1000 for VPO.

SI-4.4 Minimization of root-mean-square deviation (RMSD)

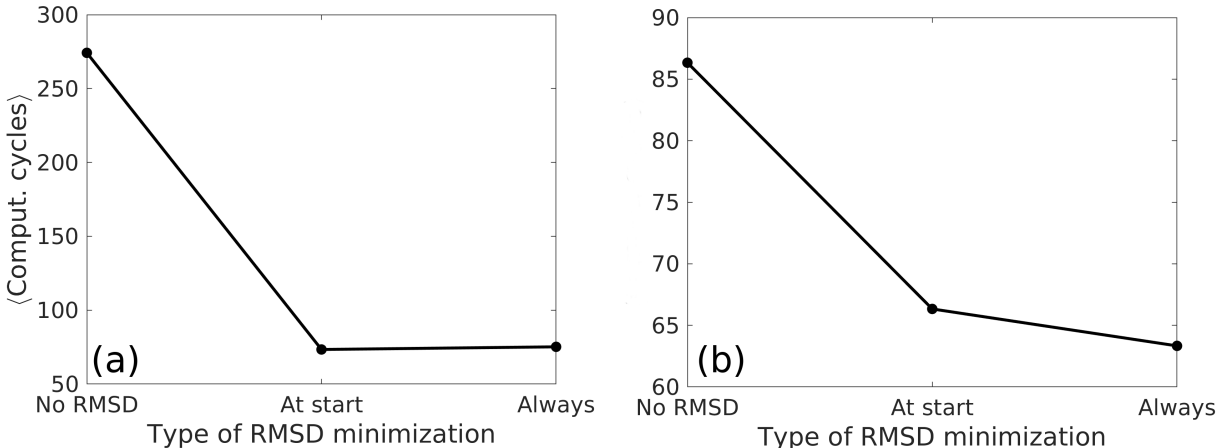


Figure 44: Computational efficiency of EW-CI-NEB calculations measured on a slightly modified benchmark set, where the product configurations have been uniformly displaced by 0.5 Å in x-direction and globally rotated by 30° ($\phi, \theta, \psi = \pi/6$). Three different sets of EW-CI-NEB calculations are then carried out; (i) without any RMSD minimization of the reactant and product configurations (ii) RMSD minimization a priori to the initial path generation of NEB and (iii) RMSD minimization is carried out, both a priori to the initial path generation and in each optimization step of EW-CI-NEB. The EW-CI-NEB calculations for systems 3 and 5 are unable to converge when no RMSD minimization is employed. In (a) the data for systems 3 and 5 is included, while in (b) it is omitted.

SI-4.5 Effect of activating climbing image

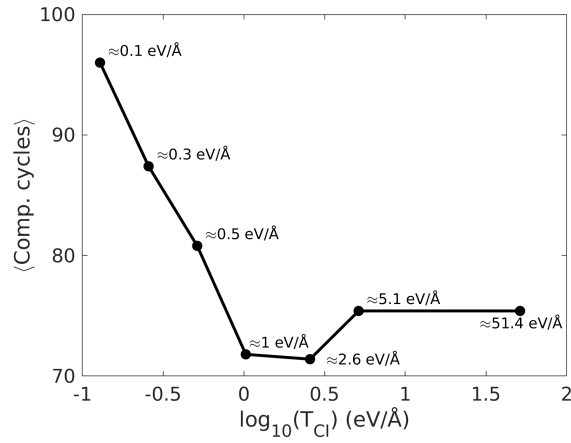


Figure 45: Computational efficiency of EW-CI-NEB/L-BFGS calculations measured on the small benchmark set, where the threshold to activate CI is varied from $\epsilon_{CI} \approx 0.1$ to 51 eV/Å

SI-4.6 Effect of the TS activation threshold

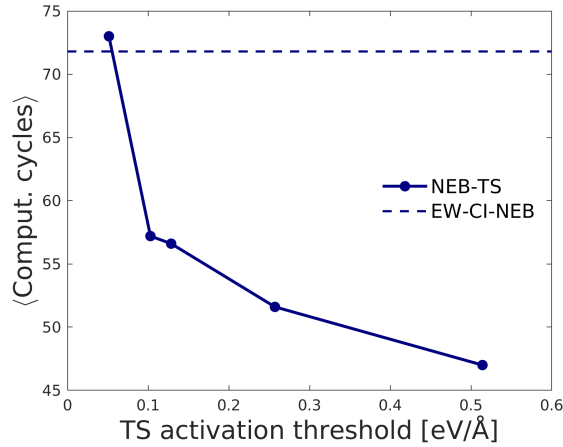


Figure 46: Computational efficiency of NEB-TS calculations using a variable TS activation threshold from $\epsilon_{max}^{TS} \approx 0.05$ to 0.5 eV/Å on the small benchmark set. For these relatively simple systems it is beneficial to activate TS in the very early stages of the EW-CI-NEB optimization.

SI-4.7 Constant trust-radius and resetting L-BFGS memory

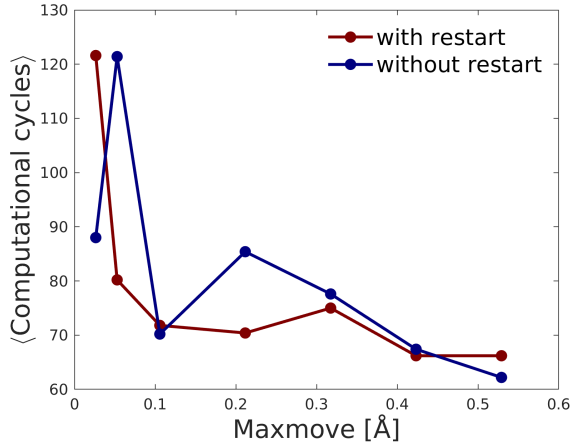


Figure 47: Computational efficiency of EW-CI-NEB/L-BFGS calculations on the small benchmark set where the allowed maximum step-size is varied, both with and without resetting the L-BFGS memory when the maximum step-size condition is invoked.

Table 9: Computational efficiency and success rate of EW-CI-NEB/L-BFGS calculations on the large benchmark set of molecular reactions. The allowed maximum step-size used is 0.2 and 0.4 a_0 , with and without resetting the L-BFGS memory when the maximum step-size condition is invoked.

$\Delta_{\text{step}}[a_0]$	Reset memory	$\langle \text{Eval.} \rangle$	Success rate [%]
0.2	True	924±603	100
0.2	False	1001±843	96
0.4	True	897±675	98

References

- (1) Birkholz, A. B. and Schlegel, H. B. Using bonding to guide transition state optimization. *J. Comput. Chem.*, **2015**, 36(15), pp. 1157–1166.
- (2) Zimmerman, P. Reliable Transition State Searches Integrated with the Growing String Method. *J. Chem. theory and Comput.*, **2013**, 9, pp. 3043–3050.
- (3) Henkelman, G.; Uberuaga, B. P.; Jónsson, H. Climbing image nudged elastic band method for finding saddle points and minimum energy paths. *J. Chem. Phys*, **2000**, 113, pp. 9901–9904
- (4) Ásgeirsson, V. (2020) https://github.com/via9a/neb_visualize.git (last visited: 10.05.2021)